7750 *Inorg. Chem.* **2009**, *48*, 7750–7764
DOI: 10.1021/ic900613p

Inorganic Chemistry
Article

Ground-State Electronic Structure of Vanadium(III) Trisoxalate in Hydrated Compounds

Kevin R. Kittilstved,*,† Lilit Aboshyan Sorgho,† Nahid Amstutz,† Philip L.W. Tregenna-Piggott,‡ and Andreas Hauser†

†*Université de Genève, Département de Chimie Physique, 30 Quai Ernest Ansermet, CH-1211 Genève, Switzerland, and* ‡*ETH Zürich and Paul-Scherrer Institute, CH-5232 Villigen PSI, Switzerland*

Received March 30, 2009

The ground-state electronic structures of $K_3V(ox)_3 \cdot 3H_2O$, $Na_3V(ox)_3 \cdot 5H_2O$, and $NaMgAl_{1-x}V_x(ox)_3 \cdot 9H_2O$ ($0 < x \leq 1$, ox = $C_2O_4^{2-}$) have been studied by Fourier-transform electronic absorption and inelastic neutron scattering spectroscopies. High-resolution absorption spectra of the $^3\Gamma(t_{2g}^2) \rightarrow {}^1\Gamma(t_{2g}^2)$ spin-forbidden electronic origins and inelastic neutron scattering measurements of the pseudo-octahedral $[V(ox)_3]^{3-}$ complex anion below 30 K exhibit both axial and rhombic components to the zero-field-splittings (ZFSs). Analysis of the ground-state ZFS using the conventional $S = 1$ spin Hamiltonian reveals that the axial ZFS component changes sign from positive values for $K_3V(ox)_3 \cdot 3H_2O$ ($D \approx +5.3$ cm^{-1}) and $Na_3V(ox)_3 \cdot 5H_2O$ ($D \approx +7.2$ cm^{-1}) to negative values for $NaMgAl_{1-x}V_x(ox)_3 \cdot 9H_2O$ ($D \approx -9.8$ cm^{-1} for $x = 0.013$, and $D \approx -12.7$ cm^{-1} for $x = 1$) with an additional rhombic component, $|E|$, that varies between ~0.8 and ~2 cm^{-1}. On the basis of existing crystallographic data, this phenomenon can be identified as due to variations in the axial and rhombic ligand fields resulting from outer-sphere H-bonding between crystalline water molecules and the oxalate ligands. Spectroscopic evidence of a crystallographic phase change is also observed for $K_3V(ox)_3 \cdot 3Y_2O$ (Y = H or D) with three distinct lattice sites below 30 K, each with a unique ground-state electronic structure.

1. Introduction

Mixed-valent polynuclear materials continue to attract considerable attention due to their possible application in future spin-based electronics technologies.[1,2] This family of magnetic materials is interesting on vastly different length scales. The single-molecule magnets have their intrinsic length scale for magnetic ordering confined to the molecular level where interesting quantum phenomena occur,[3] while for instance Prussian blue analogs span longer ordering length scales and can be influenced by various chemical perturbations as well as by light, pressure, and temperature.[4−7] These two extremes have been bridged by advances in the synthetic methods of preparing multidimensional oxalate-based networks.[4,5] Within this context, the vanadium(III) trisoxalate anion, $[V(ox)_3]^{3-}$, has received renewed attention because of its application as a pivotal component of multinuclear, mixed-valence molecular magnets.[4,6] Unfortunately, the increased focus on the ferromagnetic properties of these materials has outpaced the study of structural and magnetic correlations of the paramagnetic molecular building blocks themselves. Thus, to date, the study of the electronic structure of $[V(ox)_3]^{3-}$ has been limited to magnetic susceptibility measurements[6−8] and comparatively low-resolution electronic absorption spectroscopy.[9,10] In order fully to understand the complex magnetic properties of multicomponent systems, the ground-state electronic structures of the mononuclear species need thorough investigation. This motivated us to investigate the ground-state electronic structure of the $[V(ox)_3]^{3-}$ anion in crystalline lattices.

The highest point symmetry that the $[M(ox)_3]^{3-}$ complex can adopt is D_3. Electron paramagnetic resonance (EPR) and luminescence spectroscopies of the $[Cr(ox)_3]^{3-}$ and $[Fe(ox)_3]^{3-}$ anions in various crystalline hosts, including those studied here, demonstrate a correlation between the degree of hydration and an additional rhombic component to

*To whom correspondence should be addressed. E-mail: kevin.kittilstved@unige.ch.

(1) Bogani, L.; Wernsdorfer, W. *Nat. Mater.* **2008**, *7*, 179–186.
(2) Gatteschi, D.; Sessoli, R.; Cornia, A. *Compr. Coord. Chem. II* **2003**, *7*, 779–813.
(3) Gatteschi, D.; Sessoli, R. *Angew. Chem.* **2003**, *42*, 268–297.
(4) Min, K. S.; Miller, J. S. *Dalton Trans.* **2006**, 2463–2467.
(5) Cariati, E.; Macchi, R.; Roberto, D.; Ugo, R.; Galli, S.; Casati, N.; Macchi, P.; Sironi, A.; Bogani, L.; Caneschi, A.; Gatteschi, D. *J. Am. Chem. Soc.* **2007**, *129*, 9410–9420.
(6) Min, K. S.; Rhinegold, A. L.; Miller, J. S. *Inorg. Chem.* **2005**, *44*, 8433–8441.
(7) Machin, D. J.; Murray, K. S. *J. Chem. Soc. (A)* **1967**, 1498–1504.
(8) Figgis, B. N.; Lewis, J.; Mabbs, F. *J. Chem. Soc.* **1960**, 2480–2485.
(9) Piper, T. S.; Carlin, R. L. *J. Chem. Phys.* **1960**, *33*, 608–609.
(10) Piper, T. S.; Carlin, R. L. *J. Chem. Phys.* **1961**, *35*, 1809–1815.

 Published on Web 07/23/2009 © 2009 American Chemical Society

the zero-field splittings (ZFSs).[11−19] However, for the Kramers ions Cr^{3+} and Fe^{3+}, the rhombic ZFS term does not result in any additional splittings, and the ZFS terms do not correlate directly with the diagonal splitting of the one-electron orbitals. Octahedral V^{3+} on the other hand possesses an orbitally degenerate $^3T_{1g}$ ground term. In the strong-field limit, the energies of the orbital components of the $^3T_{1g}$ ground term correlate with the splitting of the t_{2g} orbitals, thus imparting direct information about the nature of the ligand field.[20,21]

Intraconfigurational spin-forbidden d−d transitions, for V^{3+} transitions of the type $^3\Gamma(t_{2g}^2) \rightarrow {}^1\Gamma(t_{2g}^2)$, induce little or no geometric changes between the ground and excited states. Thus, the intensity is concentrated in the electronic origins, and the resulting band widths can be on the order of 1 cm^{-1} as for V^{3+} doped into α-Al_2O_3 (Al_2O_3:V).[22−25] In this compound, the spin-forbidden d−d transitions have been studied by electronic absorption,[24,25] luminescence,[26] and Zeeman spectroscopies,[22,23] which provided a wealth of information on the ground-state electronic structure, including the direct observation and sign of the axial ZFS. As mentioned above, the analogous transitions of $[V(ox)_3]^{3-}$ have not received the same level of attention.[9] This article therefore investigates the ground- and excited-state electronic structures of the $[V(ox)_3]^{3-}$ anion in $K_3V(ox)_3\cdot 3H_2O$ (K_3V), $Na_3V(ox)_3\cdot 5H_2O$ (Na_3V), $NaMgV(ox)_3\cdot 9H_2O$ (NaMgV), and 1.3% V^{3+} diluted in $NaMgAl(ox)_3\cdot 9H_2O$ (NaMgAl:V) single crystals by high-resolution Fourier-transform (FT) absorption and inelastic neutron scattering (INS) spectroscopies. The small inhomogeneous line widths, Γ_{inh}, of the spin-forbidden d−d bands of V^{3+} allow us to resolve and analyze both axial *and* rhombic distortions of the lattices. The INS data agree with the ZFS values observed by FT absorption spectroscopy, thus supporting our assignment that the ZFSs originate from the $^3T_{1g}$ ground-state multiplet.

2. Previous Crystallographic and Spectroscopic Studies

Previous spectroscopic studies of Cr^{3+}- and Fe^{3+}-doped NaMgAl (nomenclature in analogy to the above definitions) demonstrated that the simple descriptions of axial distortions alone were not adequate to reproduce the experimentally observed ZFSs, requiring the additional consideration of rhombic terms.[11,12,14−17] The EPR spectra of Cr^{3+} and Fe^{3+} doped into K_3Al and NaMgAl lattices showed differences in the rhombicity[27] of the site symmetry of their respective ground-state electronic structures that are unique to each host lattice.[11,14,15,19,28] These lattices manifest the rhombic splittings as a result of their space group, cation disorder, crystal packing, and water content. Another interesting observation from previous EPR studies is that the sign of the axial ZFS parameter also changes sign for Cr^{3+}, as deduced from the g anisotropy[29] ($g_\parallel > g_\perp \rightarrow D > 0$ in K_3Al and Na_3Al; $g_\parallel < g_\perp \rightarrow D < 0$ in NaMgAl:Cr).[11,19]

The reversible rhombic-to-axial conversion of the $[Cr(ox)_3]^{3-}$ site symmetry in the $9H_2O$ and $8H_2O$ forms of NaMgAl:Cr has been studied extensively by EPR and electronic absorption spectroscopy. While the ZFS of the $^4A_2$ ground state of the Cr^{3+} does not change between the rhombic and axial forms of this system, the ^2E splittings change significantly from 20 cm^{-1} in the $9H_2O$ compound to <2 cm^{-1} in the $8H_2O$ compound.[11,19] Schönherr et al. studied the low-temperature polarized absorption spectra of the partially dehydrated $NaMgAl:Cr(ox)_3\cdot 8H_2O$ compound with strict D_3 site symmetry within the framework of the angular overlap model and showed that the splittings of the doublet and quartet bands are very sensitive to the angular geometry of the first coordination sphere.[28] Recent hole-burning spectroscopy of the R lines of NaMgAl:Cr has elucidated the major role played by one free water molecule lying along a C_2 axis in the lattice that provides an efficient mechanism for creating persistent spectral holes when partially deuterated.[17,18]

There is thus a mounting body of spectroscopic evidence demonstrating that low-symmetry distortions are active in the above-mentioned lattices. Since we actually do know the crystal structures of some of these compounds, in particular of the aluminum host lattices and of the neat chromium compounds, we can describe the origin of the rhombic distortions of hydrated trisoxalatometallates directly from reported structures. The crystal structures of the corresponding $[V(ox)_3]^{3-}$ compounds have not been determined in detail, except for K_3V, which was found to be isostructural to the Al and Cr analogs.[6,30] Neither the preparations nor the crystal structures of Na_3V and NaMgV have been reported to date, but powder X-ray diffraction data (see the Supporting Information) indicate that Na_3V is isostructural to Na_3Cr and Na_3Al[31] and that NaMgV is isostructural to NaMgCr and NaMgAl.[18] Thus, we shall assume the low-symmetry distortions in the V compounds to be similar to those in the Cr and Al analogs. A schematic depiction of the relevant structural distortions of the $[M(ox)_3]^{3-}$ coordination octahedron is shown in Figure 1. ORTEP representations of the specific distortions of K_3V and Na_3Cr are shown in Figure S1 in the Supporting Information. The parameters describing these distortions were derived from the published structures,[6,18,30] and the corresponding values are given in Table 1.

More specifically, the K_3M (M = V, Cr, Al) compounds crystallize in the $P2_1/c$ space group and exhibit cooperative disorder in one of the K^+ ions and one of the hydrate molecules.[6,30] The effect of H-bonding in K_3V on the oxalate

(11) Bernheim, R. A.; Reichenbecher, E. F. *J. Chem. Phys.* **1969**, *51*, 996–1001.
(12) Coleman, W. F. *J. Lumin.* **1975**, *10*, 163–169.
(13) Coleman, W. F. *J. Lumin.* **1975**, *10*, 72–76.
(14) Doetschman, D. C. *J. Chem. Phys.* **1974**, *60*, 2647–2653.
(15) Doetschman, D. C.; McCool, B. J. *Chem. Phys.* **1975**, *8*, 1–16.
(16) Otsuka, T.; Sekine, A.; Ohashi, Y.; Kaizu, Y. *Bull. Chem. Soc. Jpn.* **1992**, *65*, 3378–3385.
(17) Riesen, H.; Hughes, J. L. *Chem. Phys. Lett.* **2003**, *372*, 563–568.
(18) Riesen, H.; Rae, A. D. *Dalton Trans.* **2008**, 4717–4722.
(19) Kawasaki, Y.; Forster, L. S. *J. Chem. Phys.* **1969**, *50*, 1010–1013.
(20) Tregenna-Piggott, P. L. W.; Carver, G. *Inorg. Chem.* **2004**, *43*, 8061–8071.
(21) Beaulac, R.; Tregenna-Piggott, P. L. W.; Barra, A.-L.; Weihe, H.; Luneau, D.; Reber, C. *Inorg. Chem.* **2006**, *45*, 3399–3407.
(22) Sakatsume, S.; Kanda, E. *Sci. Rep. Res. Inst., Tohoku University, Ser. A, Suppl.* **1966**, *18*, 514–522.
(23) Sakatsume, S.; Tsujikawa, I. *J. Phys. Soc. Jpn.* **1964**, *19*, 1080.
(24) Pryce, M. H. L.; Runciman, W. A. *Disc. Faraday Soc.* **1958**, *26*, 34–42.
(25) McClure, D. S. *J. Chem. Phys.* **1962**, *36*, 2757–2779.
(26) Reber, C.; Güdel, H. U. *Chem. Phys. Lett.* **1989**, *154*, 425–431.
(27) The rhombicity is defined as the relative ratio of the rhombic and axial components of the zero-field-splittings.
(28) Schönherr, T.; Spanier, J.; Schmidtke, H.-H. *J. Phys. Chem.* **1989**, *93*, 5969–5972.
(29) Boča, R. *Struct. Bonding* (*Berlin*) **2006**, *117*, 1–264.
(30) Taylor, D. *Aust. J. Chem.* **1978**, *31*, 1455–1462.
(31) Bulc, N.; Golic, L.; Siftar, J. *Vestn. Slov. Kem. Drus.* (*Bull. Slovenian Chem. Soc.*) **1982**, *29*, 211–225.

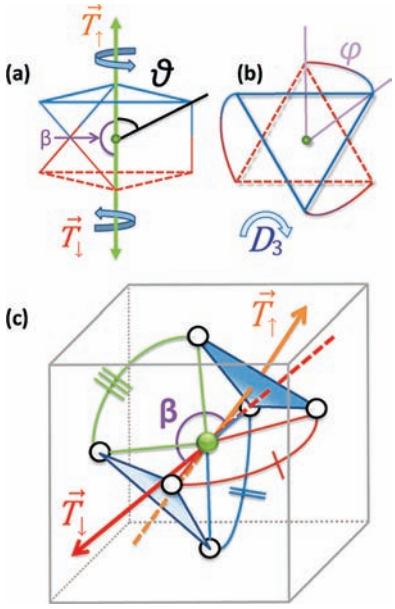

Figure 1. Schematic diagrams of the various structural distortions from cubic symmetry by the trigonal field from tris-bidentate coordination. The various parameters that define the distorted octahedron are given in a and b. The full depiction of the $[V(ox)_3]^{3-}$ bonding is shown in c. The curved lines connecting the oxygen atoms denote the chelating oxalate ligand, and the different marks mean they are inequivalent (i.e., different bond lengths, bite angles, polar and twist angles, etc.) and nonplanar (torsion angle, $\gamma \neq 0$). The bend angle, β, between the inequivalent trigonal vectors is shown and deviates from 180° for all $[V(ox)_3]^{3-}$ compounds studied. The complex has been placed in a cube to exaggerate the deviation from octahedral symmetry for the crystallographic site of the V^{3+} ion in hydrated trisoxalate compounds.

ligands was revealed by inspection of the crystal structure.[6] There are two water molecules with oxygen atoms (O_{aqua}) within 3.0 Å of different chelating oxygen atoms from the same oxalate ligand. The expected short H bonds from these water molecules perturb the oxalate bite angle, α, and increase the torsion angle, γ, defined by the chelating oxygen atoms through the C−C backbone. When $\gamma \neq 0$, the planarity of the oxalate ligand is broken, thus directly affecting the π-bonding interactions, such as phase coupling, by disrupting the conjugated π system of the oxalate.[32] More importantly, the σ-bonding interactions can be perturbed by variations in the M−O−C bond angle as rationalized by the concept of misdirected valency.[33−35] Furthermore, the V−O bond lengths, r, for a given perturbed oxalate ligand differ by up to 0.08 Å.[6] Thus, these various geometric distortions clearly provide a rhombic ligand field to the V^{3+} ion for K_3V (see Table 1).

The Na_3M (M = Cr, Al) compounds crystallize in the $C2/c$ space group with eight formula units per unit cell.[31] There is also disorder of one of the Na^+ ions, which is equally distributed over two lattice sites. The expected H-bonding in this compound is different than in the potassium salts due to the increased water content. This results in at least one V-chelating oxygen atom (O_{ox}) from different oxalate ligands having $O_{aqua}-O_{ox}$ distances within 3.0 Å. Although there is a difference in the H-bonding between the lattices, the end effects on the oxalate ligands are similar with respect to bite, torsion, and bending angles (see Table 1).

NaMgAl crystallizes in the 2D-layered honeycomb structure ($P3c1$ space group) with $[NaAl(ox)_3]^{2-}$ units making up the honeycomb, $[Mg(H_2O)_6]^{2+}$ sitting in the voids of the honeycomb sheet, and the remaining three waters occupying sites between the honeycomb layers. The crystal structure of this controversial system has been reinvestigated recently in more detail,[18] and the expected H-bonding involves every free and Mg^{2+}-bound water molecule with each oxalate ligand. The $[Al(ox)_3]^{3-}$ complex in NaMgAl is more isotropic in the first coordination environment by comparing the small deviations of the mean bond length, $\bar{r}$, and polar angle, $\bar{\theta}$, with the other lattices studied. Yet the 3-fold symmetry in NaMgAl is lifted by comparatively large torsion angles of the oxalate ligands. These torsions introduce large anisotropic bonding interactions and will be discussed in more detail in section 6.2. The bite angle for all of the compounds studied is less than cubic ($\alpha < \alpha_{cube} = 90°$), which requires the twist angle to be $\varphi < \varphi_{cube} = 60°$. The deviation from 180° for the angle, β, between the arbitrarily defined "upper" and "lower" trigonal axes, designated as $\vec{T}_\uparrow$ and $\vec{T}_\downarrow$, respectively, removes the C_3 and C_2 symmetry operations of the chromophore leaving only C_1 site symmetry. A comparison of β reveals a higher degree of deviation from D_3 symmetry for the potassium and sodium salts compared to NaMgAl (see Figure 1) and is responsible for the large deviations on $\bar{\theta}$ for K_3V.

3. Theory

For octahedrally coordinated vanadium(III) complexes, interelectronic repulsion and the cubic ligand field are large compared to spin−orbit coupling, resulting in ligand-field terms with well-defined spin and orbital angular momenta. The energies and magnetic response of the low-lying levels can therefore be rationalized using an effective Hamiltonian operating within the states of the $^3T_{1g}$ ground term. Following Abragam and Pryce, the manifold may be treated as an orbital triplet with a fictitious angular momentum $\tilde{L} = 1$ and an effective orbital g value, A, depending on the mixing of the $^3T_{1g}(F)$ and $^3T_{1g}(P)$ via the cubic ligand field.[36] In the absence of an applied magnetic field, the Hamiltonian can be written as

$$\hat{H}_{LF} = \Delta_{ax}\left[\hat{L}_z^2 - \frac{1}{3}L(L+1)\right] + \Delta_{rh}[\hat{L}_x^2 - \hat{L}_y^2] - A\lambda\mathbf{L}\cdot\mathbf{S} \quad (1)$$

where Δ_{ax} and Δ_{rh} are axial and rhombic splitting parameters, respectively, which also absorb the effect of electronic repulsion, λ is the spin−orbit coupling constant, and A takes a value between 1.0 (strong ligand field) and 1.5 (weak ligand field). The explicit form of the matrix is given in Appendix A. When analyzing the experimental splittings of the $^3T_{1g}$ ground term, the smallest energy difference between the three orbital components is taken as $2|\Delta_{rh}|$; thus, the largest splitting is always Δ_{ax}. A schematic energy-level diagram of the $^3T_{1g}$ ground term and relevant excited states with descending symmetry from O_h to C_2 is shown in Figure 2.

(32) Atanasov, M. A.; Schonherr, T.; Schmidtke, H. H. *Theor. Chim. Acta* **1987**, *71*, 59–73.
(33) Deeth, R. J.; Duer, M. J.; Gerloch, M. *Inorg. Chem.* **1987**, *26*, 2578–2582.
(34) Duer, M. J.; Fenton, N. D.; Gerloch, M. *Int. Rev. Phys. Chem.* **1990**, *9*, 227–280.
(35) Liehr, A. D. *J. Phys. Chem.* **1964**, *68*, 665–722.
(36) Abragam, A.; Pryce, M. H. L. *Proc. R. Soc. London, Ser. A* **1951**, *205*, 135–153.

Table 1. Summary of Selected Crystallographic Parameters of Trisoxalatometallate Compounds[a]

crystallographic parameters	$K_3V\cdot 3H_2O$	$K_3Cr\cdot 3H_2O$	$Na_3Cr\cdot 5H_2O$	$NaMgAl\cdot 9H_2O$	trigonal
space group	$P2_1/c$	$P2_1/c$	$C2/c$	$P3c1$	
T collection (K)	213	> 283	> 283	200	
M^{3+} symmetry	C_1	C_1	C_1	C_1	D_{3d}
mean M−O, r (Å)	2.007(36)	1.969(13)	1.972(8)	1.903(4)	
bend, β,$\angle\vec{T}_\uparrow - V\ \vec{T}_\downarrow$ (deg)	176.5	178.5	178.8	179.5	180
mean polar angle, ϑ,$\angle O-V-\vec{T}_\uparrow/\vec{T}_\downarrow$ (deg)	54.7 ± 2.9	55.50 ± 0.87	55.99 ± 1.14	55.68 ± 0.37	54.74
bite angles, $\bar{\alpha}$,$\angle O_\uparrow-V-O_\downarrow$ (deg)	80.34	81.75	82.43	84.47	90
	80.05	82.51	82.80	84.71	90
	80.09	82.48	82.24	84.15	90
torsion angles, γ,$\angle O_\uparrow-C_\uparrow-C_\downarrow$ (deg)	6.32	10.05	9.70	0.39	0
	3.78	7.89	3.44	−6.08	
	3.59	7.44	4.36	6.06	
	$\sigma(\bar{\gamma})$ = 1.24	*1.14*	*2.76*	*4.96*	*0*
∠V−O−C (deg)	115.9 ± 1.2	114.3 ± 0.6	114.3 ± 0.3	114.5 ± 0.4	
reference	6	30	31	18	

[a] For each compound, the trivalent metal occupies a general position with C_1 symmetry. Inspection of the atomic arrangement in the compounds reveals inequivalence in the M−O bond lengths, O−M−O bite angles, and torsion angles. The standard deviation in the mean value for the torsion angles, $\sigma(\bar{\gamma})$, is given in italics. The pseudo-trigonal axis can be determined by the vector made by the central V^{3+} ion and the centroid defined by the O_{ox} ligands above ($\vec{T}_\uparrow$) and below ($\vec{T}_\downarrow$) the "mirror" plane bisecting the oxalate ligands.

In the majority of vanadium(III) complexes, the anisotropic ligand field yields an orbital singlet ground term whose separation from the higher-lying states is large compared to the product, $A\lambda$. In this instance, it is convenient to model the energies of the three lowest-lying levels using the conventional spin Hamiltonian:

$$\hat{H}_s = D\left[\hat{S}_z^2 - \frac{1}{3}S(S+1)\right] + E[\hat{S}_x^2 - \hat{S}_y^2] \qquad (2)$$

operating within the states of the $S = 1$ multiplet. The axial and rhombic spin-Hamiltonian parameters D and E may be expressed in terms of the parameters given in eq 1 using standard methods of perturbation theory. In the common instance when Δ_{ax} is positive (Δ_{ax}^+) and $\Delta_{ax}^+ \gg A\lambda \gg |\Delta_{rh}|$, we find

$$D \approx \frac{(A\lambda)^2}{\Delta_{ax}^+} \qquad (3a)$$

$$|E| \approx \frac{|\Delta_{rh}|}{\Delta_{ax}^+} D \qquad (3b)$$

$$\frac{|E|}{D} \approx \frac{|\Delta_{rh}|}{\Delta_{ax}^+} \leq \frac{1}{3} \qquad (3c)$$

For small values of $|\Delta_{rh}|$, the parameter E is predicted to increase linearly with $|\Delta_{rh}|$, in accordance with the numerical calculations to be presented and discussed in section 5.3.

The ^3E component of the $^3T_{1g}$ multiplet becomes the ground term when Δ_{ax} is negative (Δ_{ax}^-), a scenario that has not been reported for any trigonally distorted vanadium(III) complex to date. When $|\Delta_{ax}^-| \gg A\lambda$ and $\Delta_{rh} = 0$, the six spinors arising from the ^3E ground term are $E < E < A_1 < A_2$, as shown in Figure 2. The addition of a large Δ_{rh} parameter tends to group these spinors into two $S = 1$ orbital singlets. When $|\Delta_{ax}^-| \gg |\Delta_{rh}| \gg A\lambda$, the energies of the three lowest-lying spinors can be parametrized using the spin Hamiltonian given by eq 2. The expressions derived for the spin-Hamiltonian parameters using perturbation theory for Δ_{ax}^- are

$$D \approx \frac{\Delta_{ax}^-}{|\Delta_{rh}|}|E| \qquad (4a)$$

$$|E| \approx \frac{(A\lambda)^2}{2(|\Delta_{rh}| - \Delta_{ax}^-)} \qquad (4b)$$

$$\left|\frac{E}{D}\right| \approx \left|\frac{\Delta_{rh}}{\Delta_{ax}^-}\right| \leq \frac{1}{3} \qquad (4c)$$

The parameters Δ_{ax} and Δ_{rh} absorb the effects of both the diagonal and off-diagonal anisotropic ligand fields. Counter to the expectations from considerations of orbital overlap, trigonally compressed homoleptic complexes formed from linearly ligating ligands will yield a $^3A_2$ trigonal ground term due to configuration interaction via the off-diagonal trigonal field.[37] However, the corresponding splitting is small—less than 100 cm^{-1} for $\theta = 55.5°$—and is dwarfed by the diagonal trigonal field when the ligands are nonlinearly ligating. This is the case for trisoxalate coordination, for which Atanasov and co-workers[32] showed that the π interaction normal to the plane of the bidentate ligand is larger than the interaction in the plane. In addition, the small bite angle of the oxalate ligand can change the sign of the Δ_{ax} splitting that is expected to result in a negative value for NaMgAl:V (i.e., $^3E < {}^3A_2$).[38] A large anisotropic ligand field can therefore result if the $[V(ox)_3]^{3-}$ anion is sufficiently distorted, a measure of which is obtained by determination of the ZFS parameters given in eqs 3 and 4.

4. Experimental Methods

4.1. Materials. The following chemicals were used as received: VCl_3 (99%, Alfa Aesar), V_2O_5 (99.6%, Alfa Aesar), S (99.998%, Sigma Aldrich), H_2SO_4 (96%, Reactolab SA, Verney, Switzerland), CS_2 (> 99.5%, Fluka), $Al_2(SO_4)_3\cdot 6H_2O$ (≥98.0%, Fluka), $NaOH\cdot H_2O$ (99.996%, Alfa Aesar), MgO (≥98.0%, Fluka), $Ba(OH)_2\cdot 8H_2O$ (≥98.0%, Fluka), $Na_2C_2O_4$ (> 99.5%, Fluka), $K_2C_2O_4$ (≥99%, Fluka), and $H_2C_2O_4\cdot 2H_2O$ (≥99.0%, Fluka).

4.2. Synthesis of $K_3V(ox)_3\cdot 3H_2O$ (K_3V) and $Na_3V(ox)_3\cdot 5H_2O$ (Na_3V) Single Crystals. The potassium compound was

(37) Tregenna-Piggott, P. L. W.; Best, S. P.; Güdel, H. U.; Weihe, H.; Wilson, C. C. *J. Solid. St. Chem.* **1999**, *145*, 460–470.
(38) Kittilstved, K. R.; Hauser, A. Unpublished results.

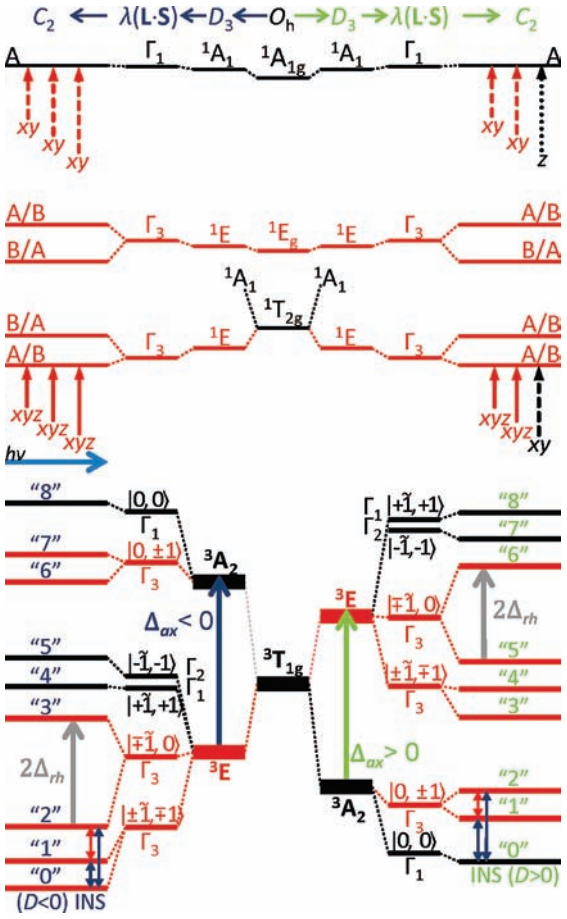

Figure 2. Splitting diagram of the states arising from the t_{2g}^2 electronic configuration with descending symmetry from $O_h \rightarrow D_3 \rightarrow \lambda(\mathbf{L}\cdot\mathbf{S}) \rightarrow C_2$. States are assigned on the basis of the nomenclature defined by eqs 1 and 6a−c, and the expected polarizations are given for the $D_3+\lambda(\mathbf{L}\cdot\mathbf{S})$ pseudo-symmetry case (eq 6d−g). The rhombic distortion removes all remaining degeneracy of the $^3T_{1g}$ ground term, and the corresponding spinor levels are numbered beginning with "0". Energies are not drawn to scale.

prepared according to the modified literature method of Min and Miller.[4] The preparation of the sodium compound has not been reported previously. The compound was prepared by modifying the preparation for K_3V by substituting stoichiometric amounts of $Na_2(ox)$ for $K_2(ox)$. Single crystals were grown by slow evaporation from supersaturated aqueous solutions kept in the dark. The potassium compound crystallized into flat prismatic platelets with millimeter dimensions, and the sodium compound crystallized in long, hexagonal needles. Green/blue dichroism was observed under polarized light for both compounds. Results from combustion analysis are as follows: K_3V (theoretical: C = 14.82%, H = 1.24%; actual: C = 14.62%, H = 1.25%), Na_3V (theoretical: C = 15.20%, H = 2.13%; actual: C = 15.40%, H = 1.90%). Thermogravimetric analysis confirmed three and five water molecules per formula unit for K_3V and Na_3V, respectively (Figure S2, Supporting Information). X-ray powder diffraction indicates Na_3V to be isostructural with Na_3Cr and Na_3Al (Figure S3, Supporting Information).

4.3. Synthesis of $NaMg[Al_{1-x}V_x(ox)_3]\cdot 9H_2O$ (NaMgAl:V) and $NaMgV(ox)_3\cdot 9H_2O$ (NaMgV) Single Crystals. The NaMgAl:V compound was prepared from a modified literature method[39] with the only change being the vanadium source, VCl_3. First, the $NaMgAl(ox)_3$ aqueous solution was prepared according to eq 5, with care taken to ensure complete removal of any sulfate anions from the growth solution before adding the VCl_3.

$$Al_2(SO_4)_3 + 6H_2C_2O_4 + 2NaOH + 2MgO + 3Ba(OH)_2 \rightarrow 2NaMgAl(ox)_3(aq) + 3BaSO_4(s) \quad (5)$$

After filtering the $BaSO_4$ precipitate, the desired amount of VCl_3 was added to the solution. Crystals were grown from supersaturated solutions by slow evaporation. The crystals were hexagonal needles with dimensions on the order of millimeters and displayed the blue/green dichroism when viewed under polarized light. Combustion analysis results are as follows: theoretical, C = 14.40%, H = 3.63%; actual, C = 14.81%, H = 3.61%. The V^{3+} concentration in the diluted crystals was determined by optical spectroscopy.

The preparation of neat NaMgV has not been reported previously and attempts to prepare it using VCl_3 produced Na_3V. We were successful in preparing it, however, from a slight modification of the literature method[39] for preparing NaMgAl with $V_2(SO_4)_3$ as the V^{3+} precursor. $V_2(SO_4)_3$ powder was prepared by a literature method.[40] Briefly, under constant stirring, $V_2(SO_4)_3$ (1.9504 g, 5.0 mmol) was added to 20 mL of water at 60 °C. To this, 10 mL of a 3.0 M $H_2C_2O_4$ (30 mmol) solution was added slowly. This solution was stirred at 60 °C for 6 h and overnight at room temperature. The small amount of undissolved $V_2(SO_4)_3$ was filtered, and the solution was reheated to 60 °C. Under constant stirring, MgO (0.403 g, 10 mmol) was added. Once complete dissolution occurred, $NaOH\cdot H_2O$ (0.58 g, 10 mmol) dissolved in 1 mL of H_2O was added. After a hot, filtered solution of $Ba(OH)_2\cdot 8H_2O$ (4.732 g, 15 mmol) was added, the cloudy solution was allowed to cool to room temperature without stirring for 3 h. The white $BaSO_4$ precipitate was filtered by water aspiration, and the green growth solution was concentrated by rotary evaporation to ~1/3 of its original volume. After a week of slow evaporation under a flow of N_2 gas in the dark, we obtained large blue/green dichroic needles with millimeter dimensions. Combustion analysis results are as follows: theoretical, C = 13.74%, H = 3.46%; actual, C = 13.98%, H = 3.33%. Thermogravimetric analysis confirmed the water content of nine molecules per formula unit (Figure S2. Supporting Information). The crystallographic phase of $NaMgV\cdot 9D_2O$ was confirmed to be isostructural to NaMgAl by comparison of the experimental powder X-ray diffraction pattern to the simulated pattern of NaMgAl (Figure S4, Supporting Information).

Deuterated samples of K_3V, Na_3V, and NaMgV were prepared for INS measurements. Since the only protons come from the waters of crystallization, the preparation of deuterated samples is achieved by simply replacing D_2O for H_2O as the solvent in the growth solution. The deuterated powders were prepared by partially evaporating supersaturated D_2O solutions using a rotary evaporator. This procedure of dissolving the compounds in D_2O and partially evaporating the solutions was performed three times for each sample to ensure that the large majority of H_2O molecules in the compounds were replaced by D_2O. The fully deuterated samples were allowed to dry by gravity filtration overnight in the dark and were stored at < 5 °C.

4.4. Electronic Absorption Spectroscopy. Variable-temperature and polarized absorption spectra were recorded using a Fourier-transform spectrometer with appropriate light sources, beam splitters, and detectors to cover the spectral range from 6000 to 30 000 cm^{-1} with a spectral resolution of 0.5 cm^{-1} (Bruker IFS-66). For the polarized spectra around 480 ± 15 nm of K_3V only, we employed a 0.85 m double-monochromator (Spex 1404) to disperse the transmitted light onto a 2048 × 512 pixel CCD camera with 13.5 × 13.5 μm pixel dimensions (Roper

(39) Lipkowski, J.; Herbich, J. *Roczniki Chemii: Ann. Soc. Chim. Polonorum* **1975**, *49*, 853–857.

(40) Zatko, D. A.; Kratochvil, B. *Anal. Chem.* **1965**, *37*, 1560–1562.

Scientific). The polarized spectra were collected with respect to the parent D_3 molecular axis of the $[V(ox)_3]^{3-}$ chromophore, which coincides nearly with the crystallographic *c* axis for all compounds studied except for K_3V (< 10° of the *a* axis).[6] Room-temperature spectra were collected on a dual-beam spectrophotometer equipped with dual polarizers (Varian Cary 5000). Crystalline samples were oriented with a polarized microscope and mounted on copper apertures and placed in an optical closed-cycle cryostat capable of reaching base temperatures of either 10 K in an atmosphere of He exchange gas (Oxford Instruments, CCC1100T) or 4.4 K (Sumitomo SHI-4-5). Crystals placed in the Sumitomo cryostat were mounted with heat-conducting silver glue and evacuated to ca. 10^{-5} mbar. Exposing the crystals to high vacuum conditions leads to disintegration at room temperature. Therefore, the samples were first cooled to ~250 K with a modest vacuum of ~50 mbar. Once 250 K was reached, the pressure was lowered to ca. 10^{-5} mbar by turbomolecular pumping, and then they were cooled to the base temperature. An additional copper shroud with ~2-cm-diameter apertures was machined to stabilize the base temperature. Deconvolution of the spectra was performed using the multiple-peak and global fitting procedures in Igor Pro, version 6.0 (WaveMetrics, Inc.).

4.5. Inelastic Neutron Scattering. Oxalate-based compounds are ideal for study by neutron-based techniques due to their lack of protons, as compared to other bidentate ligands, such as 2-2′-bipyridine ($(C_5H_4N)_2$) or ethylenediamine ($C_2H_2(NH_2)_2$). Approximately 7 g of deuterated powders of K_3V, Na_3V, and NaMgV were loaded into 12-mm-diameter hollow aluminum measurement cylinders, sealed under a He atmosphere, and placed in a standard ILL Orange cryostat for temperature control. INS measurements were carried out on the direct-geometry time-of-flight spectrometer FOCUS[35] and the inverted-geometry time-of-flight spectrometer MARS,[36] both located at the Paul Scherrer Institute. For the FOCUS experiments, an empty aluminum can of the same dimensions as the sample holder was measured and the spectrum subtracted from that of the sample; the detector efficiency correction was performed using data collected from vanadium. A wavelength of 5.85 Å was employed, affording a resolution of 0.36 cm^{-1} at the elastic peak with an energy window extending to ~12 cm^{-1} on the neutron-energy-loss side of the spectrum. For the MARS[41,42] experiments, energy selection was achieved by selecting the 006 and 002 MICA reflections. At a given energy transfer, the resolution was varied by concomitantly changing the speed of the pulse-producing chopper and the sample-analyzer-detector angle, this being a unique feature of the instrument.

Instrument control, data reduction, and analysis were accomplished using software featured within the DAVE program package.[43]

5. Results

5.1. Electronic Absorption Spectroscopy. The room-temperature electronic absorption spectrum of an aqueous solution of K_3V is shown in Figure 3a. Several broad absorption features are observed in the visible region centered at 16 550, 23 650(sh), and 28 850 cm^{-1} and assigned to the spin-allowed d−d transitions from the $^3T_{1g}$ ground state to the $^3T_{2g}$, $^3T_{1g}$(P), and overlapping $^1\Gamma(t_{2g}e_g)$ and $^3A_{2g}$ excited states of O_h parentage, respectively. Another broad and intense absorption band beginning at 36 300 cm^{-1} is assigned to a ligand-to-metal charge-transfer transition.

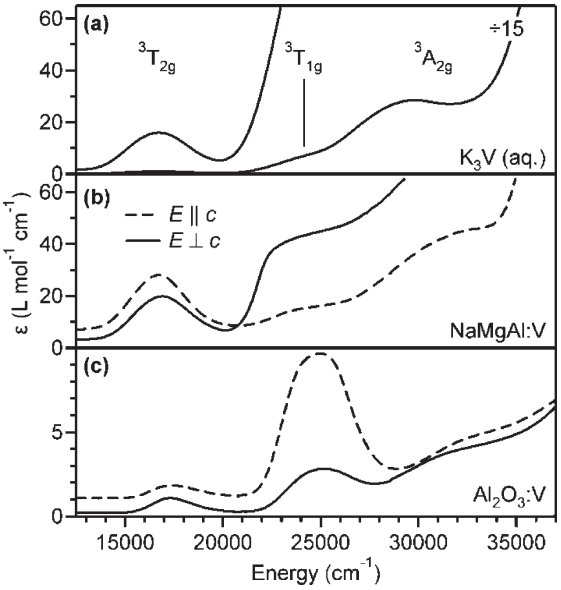

Figure 3. (a) Electronic absorption spectrum of an aqueous K_3V solution. Polarized electronic absorption spectra of (b) a 3.2-mm-thick single crystal of NaMgAl:V (6.6% V^{3+}) and (c) a 5-mm-thick single crystal of Al_2O_3:V (0.8% V^{3+}, dashed line). Polarization defined with the electric field vector, *E*, parallel (dashed) or perpendicular (solid) to the crystallographic (and molecular) unique axis. Spectral band assignments are based on the parent O_h symmetry. All spectra collected at room temperature.

The room-temperature polarized electronic absorption spectrum of a NaMgAl:V (6.6% V^{3+}) single crystal is shown in Figure 3b. Several broad absorption features of varying extinction are observed in the visible region and assigned to transitions from the $^3T_{1g}$ ground state to the trigonally split excited states as for the solution spectrum in Figure 3a. The energies and assignments of the polarized bands are given in Table 2. The extinction ratio for the polarized $^3T_{2g}$ transition at ~16 800 cm^{-1} is $\varepsilon_{\parallel}/\varepsilon_{\perp} \approx 1.35$, in agreement with the previously reported value of 1.3 by Piper and Carlin.[10] Similar absorption features were observed in the single-crystal absorption spectrum of Al_2O_3:V (0.8% V^{3+}), but at higher energies with weaker intensities (see Figure 3c for a direct comparison).[25,44]

Upon cooling the $[V(ox)_3]^{3-}$-containing compounds to cryogenic temperatures, narrow features appear in the near-IR and in the visible region between the $^3T_{2g}$ and $^3T_{1g}$(P) absorption features. The band in the near-IR region we will refer to as the "NIR line" to designate the spectral region of the transition. The band in the visible will be termed the "BG line" as it occurs at blue/green wavelengths. Below 30 K, these absorption features narrow and their extinction coefficients become comparable to that of the $^3T_{2g}$ transition. The corresponding low-temperature polarized single-crystal absorption spectra of the NIR and BG lines are shown in Figures 4 and 5, respectively. The oscillator strengths of ~10^{-8} and ~10^{-7} and the comparative sharpness of these lines identify them as spin-forbidden transitions from the $^3T_{1g}$ ground state to the $^1T_{2g}$ and $^1A_{1g}$ excited states, respectively.

Figure 4a shows the unpolarized overview FT-absorption spectra of the NIR lines below 4.2 K of K_3V, Na_3V, NaMgV,

(41) Tregenna-Piggott, P. L. W.; Juranyi, F.; Allenspach, P. *J. Neutron Res*. In press.
(42) Tregenna-Piggott, P. L. W.; Juranyi, F.; Allenspach, P. *Neutron News* **2008**, *19*, 20–24.
(43) Tregenna-Piggott, P. L. W. MagProp (part of the NIST DAVE software suite), v2.0 (20 Oct **2008**). http://www.ncnr.nist.gov/dave (accessed July 2009).
(44) Tippins, H. H. *Phys. Rev. B* **1970**, *1*, 126–135.

Table 2. Ligand-Field Parameters Fit from the Experimental Energies of V^{3+} in NaMgAl Using the Ligand-Field Expressions Given in Appendix B[a]

parameter	NaMgAl:V	Al_2O_3:V[b]
10Dq	17733	18454
B_c	552.2	590.3
C_c	3007	2958
$\eta = B_c/B_o(= k)$	0.62	0.67
$\lambda = k\zeta_o/2S$	65	70
A	1.25	1.25

NaMgAl:V

$\Gamma(O_h)$	fitting energies	exptl	calcd
$^1T_{2g}(D)$	9590	9590(⊥)	9590
$^1E_g(D)$			9696
$^3T_{2g}(F)$	16550[c]	16700(∥)	16550
		16910(⊥)	
$^1A_{1g}(G)$		20465(⊥)	20835
$^3T_{1g}(P)$	23650[c]	−(⊥)	23650
		23575(∥)	
$^3A_{2g}(F)$		~32670(sh,∥)	34283

[a] Parameters for Al_2O_3:V calculated using the experimental energies from Reber and Güdel[26] in the absence of the trigonal approximation. We assume that the nephelauxetic ratio, η, is equivalent to the orbital reduction factor, k. The mixing coefficient was calculated from the Dq and B values following Mabbs and Machin.[50] Free ion values are B_o = 886 cm^{-1}, C_o/B_o = 4.0, and ζ_o = 210 cm^{-1}. All energies are in cm^{-1}. [b] Determined using the experimental energies from ref 26: $^1T_{2g}(D)$ = 9744 cm^{-1}, $^3T_{2g}(F)$ = 17 200 cm^{-1}, $^3T_{1g}(P)$ = 24 800 cm^{-1}. [c] Energies taken from the K_3V solution spectrum shown in Figure 3a.

and NaMgAl:V (15% V^{3+}). The rich vibronic structure observed for all of the compounds studied is not important for the current discussion and will be discussed elsewhere. For the current discussion, we will limit our analysis to the electronic origins. The NIR lines of K_3V and Na_3V are observed at ~9400 cm^{-1} but for NaMgV and NaMgAl:V are blue-shifted to ~9600 cm^{-1}. The molar extinction coefficients and line widths of these transitions are instrument-limited by the FT spectrometer, even at 0.5 cm^{-1} spectral resolution (data not shown). Similar to the spin-allowed bands, the spin-forbidden transitions also display a large degree of polarization, as evidenced in Figure 4b−e for the NIR lines. Broadly speaking, the absorption spectra show three sharp and temperature-dependent features spread over a window of ~15 cm^{-1}. In contrast, the peculiar spectra of K_3V, shown in Figure 4b, exhibit three distinct sets of these bands centered at 9370, 9400, and 9430 cm^{-1} of comparable intensities, line widths, and polarization ratios. Each set, labeled **A**, **B**, and **C** with increasing transition energy, also displays additional splittings, resulting in three peaks falling within the same range of ~15 cm^{-1}.

The energies of the NIR lines of NaMgV and NaMgAl:V (1.3% V^{3+} here and in the following) are 9610 cm^{-1} and 9590 cm^{-1}, respectively, as can be seen in the high-resolution spectra in Figure 4d,e. In addition to the two narrow features at ~9610 cm^{-1}, a very weak feature is observed at 9598 cm^{-1} in the spectrum of NaMgV. The inset to Figure 4d shows that this weak feature gains intensity with increasing temperature. Spectral deconvolution of each electronic origin in Figure 4b−e using three Voigt band profiles was performed, and the resulting transition energies and average peak line widths (fwhm, full-width at half-max) are given in Table 3. The energy differences of the NIR and BG lines are given in Table 4

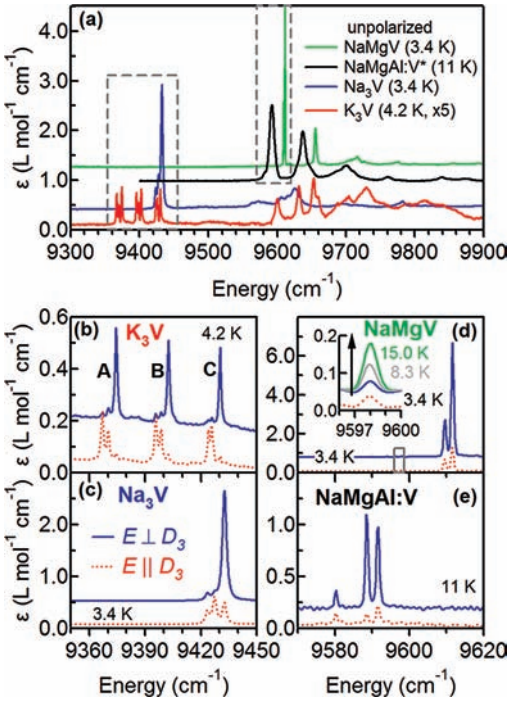

Figure 4. Low-temperature FT-absorption spectra of the NIR lines of various hydrated $[V(ox)_3]^{3-}$ crystalline compounds. (a) Unpolarized overview spectra of the NIR lines. The concentration of V in NaMgAl:V in a is ~15% and in e is 1.3%. Polarized FT-absorption spectra of the lowest-energy sharp feature on an expanded scale for (b) K_3V, (c) Na_3V, (d) NaMgV, and (e) NaMgAl:V (1.3% V^{3+}). The polarization was collected with respect to the pseudo-D_3 parent symmetry of the $[V(ox)_3]^{3-}$ complex in the crystal (see text). The temperature dependence of the spectral feature at 9598 cm^{-1} is shown in the inset of d. Temperatures and polarizations are given in the figure. Note the different y scales and energy scales for the different panels.

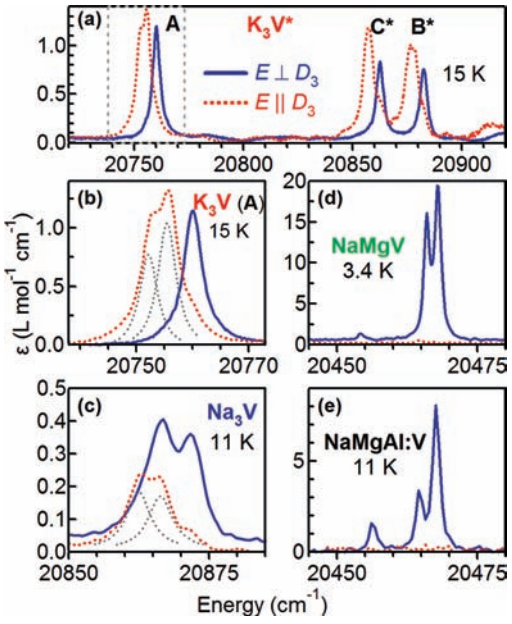

Figure 5. Low-temperature polarized FT-absorption spectra of the BG lines for the same crystals shown in Figure 4b−e. The overview polarized absorption spectra of the K_3V is shown in a and displays three distinct strong absorption bands. The detailed absorption spectra of set **A** is shown in b. The energy ranges are (a) 175 cm^{-1} and (b−e) 35 cm^{-1}. Temperatures and polarizations are given in the figure. Note the different y scales between the various panels.

using the equation $\Delta E = E_0 - E_i$, where E_0 corresponds to the highest energy peak, and i = 1 and 2. This analysis

Table 3. Experimental Energies and Average Line Widths of the NIR and BG Lines below 11 K of the Different $[V(ox)_3]^{3-}$ Compounds[a]

spectral assignment[b]		K_3V[c] set **A**	K_3V[c] set **B**	K_3V[c] set **C**	Na_3V	NaMgV	NaMgAl:V
NIR line:	i = **2**	9366.95	9395.68	9424.02	9423.54	9598.03	9580.29
$^3A(^3\Gamma(^3T_{1g}))\rightarrow$	**1**	9370.16	9398.48	9425.93	9427.39	9609.60	9588.57
$^1A(^1\Gamma(^1T_{2g}))$	**0**	9374.57	9402.67	9430.50	9432.70	9611.62	9591.55
	$\bar{\Gamma}_{inh}$	1.4(2)	1.4(1)	1.4(2)	2.8(4)	0.86(5)	0.90(3)
BG line:	i = **2**	20752.60	20875.65	20856.26	20863.1	20454.26	20456.40
$^3A(^3\Gamma(^3T_{1g}))\rightarrow$	**1**	20755.92	20878.03	20858.03	20867.0	20466.01	20464.69
$^1A(^1A_1(^1A_{1g}))$	**0**	20760.13	20882.53	20862.53	20872.2	20467.95	20467.68
	$\bar{\Gamma}_{inh}$	>4[c]	>4[c]	>4[c]	4.0(1.6)	1.3(1)	1.4(1)

[a] Spectral assignments are based on the states that arise from the $C_1(D_3(O_h))$ symmetry hierarchy in the absence of spin-orbit coupling. The splitting of the ground state is different for the compounds and designated as $^3\Gamma$. For K_3V, the three sets of absorption bands are labeled **A**, **B**, and **C** in order of increasing energy of the NIR lines (see Figure 4). Note that sets **B** and **C** do not follow the same energetic order between the NIR and BG lines on the basis of the energy splittings (see Table 4). $\bar{\Gamma}_{inh}$ is the average full-width at half-max (fwhm) for the individual peaks. All energies are in cm^{-1}. [b] The ground term in D_3 symmetry of K_3V and Na_3V is $^3A_2$ and of NaMgV and NaMgAl:V is ^3E (see section 6). [c] Spectra of the BG lines for K_3V were collected on a Spex 1404 monochromator with CCD detection (see Section 4).

Table 4. Experimental Energy Differences of the NIR and BG Lines below 11 K and INS Spectra at below 2 K for the Different $[V(ox)_3]^{3-}$ Compounds[a]

spectral parameters		K_3V[b] set **A**	K_3V[b] set **B**	K_3V[b] set **C**	Na_3V	NaMgV	NaMgAl:V
NIR line	$\Delta E_{\mathbf{0-2}}$	7.62(2)	6.98(2)	6.47(3)	9.07(2)	13.59(2)	11.26(2)
	$\Delta E_{\mathbf{0-1}}$	4.39(3)	4.17(3)	4.64(2)	4.99(1)	2.02(1)	2.98(1)
BG line	$\Delta E_{\mathbf{0-2}}$	7.53(5)	6.88(3)	6.27(6)	9.1(1)	13.69(5)	11.27(4)
	$\Delta E_{\mathbf{0-1}}$	4.21(3)	3.98(3)	4.50(5)	5.2(1)	1.94(1)	2.99(2)
INS[c]	$\Delta E_{\mathbf{0-2}}$	7.67(2)	6.84(1)	6.15(1)	9.180(1)	13.80(1)	
	$\Delta E_{\mathbf{0-1}}$	4.34(6)	3.88(1)	4.53(1)	5.340(1)	2.11(1)	
	$\bar{\Gamma}_{inh}$	0.66(4)	0.44(1)	0.40(1)	0.42(1)	0.32(1)	

[a] Differences in peak energies are taken with respect to the highest energy origin of the NIR and BG lines or from the elastic peak at 0 cm^{-1} in the INS spectra. For K_3V, the three sets of absorption bands are labeled **A**, **B**, and **C** as shown in Figures 4 and 5. $\bar{\Gamma}_{inh}$ values (fwhm) are also included for the INS transitions. All energies are in cm^{-1}. [b] Energies from the INS spectra are assigned to the various sets depending on the ΔE values from the BG line. [c] Instrument resolutions for determining the peak energies from the INS spectra were 0.10 cm^{-1}, 0.36 cm^{-1}, and 0.18 cm^{-1} for K_3V, Na_3V, and NaMgV, respectively.

reveals that the energy splittings of the NIR lines among the compounds studied are all unique, even among the different sets of peaks for K_3V.

Figure 5 shows the polarized FT-absorption spectra of the BG lines of the compounds between 20 400 and 21 000 cm^{-1}. The overview spectra of K_3V in Figure 5a display the same "tripling" phenomenon observed for the NIR lines in Figure 4a, but with different energy separations between the sets of absorption features centered at 20 760, 20 860, and 20 880 cm^{-1}. While the line widths of the individual BG lines for K_3V are larger than the NIR lines, the polarization of the bands allowed us to resolve three individual peaks for each transition, as shown in Figure 5b for set **A**. On the basis of similarity of the deconvoluted ΔE values between the NIR and BG lines for the different compounds (Figure 5c−e, Table 4), we were able to compare and identify which BG line corresponds to a given NIR line. It thus appears that the ordering of the three sets is **A** < **C** < **B** with increasing energy for the BG line. As for K_3V, the BG line for Na_3V is broadened at 11 K compared to the NIR line, but the polarized spectra allowed for three individual peaks to be resolved at similar ΔE values compared to the NIR line (Figure 5c). The resolved BG lines for NaMgV and NaMgAl:V show the strongest extinction with intensity only observed when $E \perp D_3$. The ΔE values of the BG lines for NaMgV and NaMgAl:V are in agreement with those determined for the NIR lines. The absolute energies of the BG line, however, do not follow the same energetic ordering as for the NIR lines, which is $K_3V \sim Na_3V <$ NaMgAl:V $\sim$ NaMgV. This trend is completely reversed for the energies of the BG lines.

Differences in the splittings of the NIR and BG lines are at most $\sim 3\sigma$ for a given compound (see Table 4). In addition, the average line widths of the BG lines are larger than those of the NIR lines for all of the compounds studied. The narrowest line widths, $\bar{\Gamma}_{inh}$, are observed for NaMgV and NaMgAl:V with fwhm's of $\sim$0.90 and $\sim$1.3 cm^{-1} for the NIR and BG lines, respectively.

Figure 6 shows the temperature dependence of the NIR and BG lines for K_3V. The three sets of NIR lines show drastic changes with increasing temperature. The individual peaks within each transition change in relative intensities below 20 K without shifting in energy. Upon increasing the temperature to 28 K, the sets of transitions begin to shift in energy and intensity. The spectrum collected at 39 K shows that the three sets have morphed into two broad bands centered where no intensity is observed in the 11 K spectrum. This shifting behavior with increasing temperature continues until the bands collapse into a single band above $\sim$63 K. The total integrated intensity between 9350 and 9450 cm^{-1} does not change as a function of the temperature. The same temperature behavior is observed for the BG lines with the exception that because of the larger energy separation between set **A** and sets **B** and **C** there are slight differences in the overall merging of the spectral features.

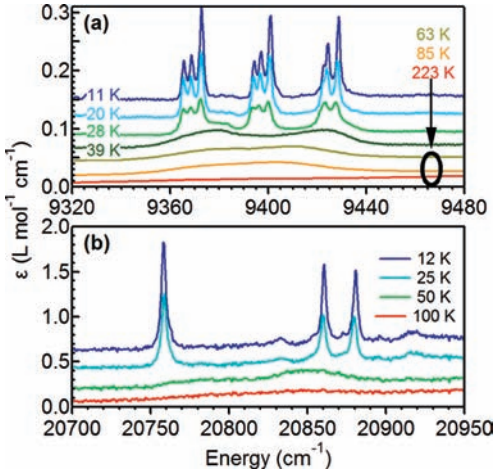

Figure 6. Temperature-dependent absorption spectra of the (a) NIR and (b) BG lines of K_3V. The spectra are unpolarized. Temperatures are given in the figure. Spectra have been vertically offset for clarity.

5.2. Inelastic Neutron Scattering. The variable-temperature INS spectra of deuterated powders of K_3V, Na_3V, and NaMgV are shown in Figure 7. The measurements were collected between 1.5 and 30 K on the time-of-flight (TOF) spectrometer FOCUS at an instrument resolution of 0.36 cm^{-1} and an energy transfer window between −16 and +12 cm^{-1}. Additional spectra using the new inverted backscattering TOF Mica analyzer high-resolution spectrometer (MARS) were collected on NaMgV (Figure 7c) and K_3V (Figure 8) with a superior instrument resolution of better than 0.2 cm^{-1}.

The INS spectra of fully deuterated NaMgV collected on FOCUS at 1.5 K show only one strong feature in the positive energy-transfer region as a shoulder on the elastic peak at ∼2 cm^{-1} (Figure 7c). The low-energy feature disappears upon raising the temperature to 30 K, while two broad peaks appear at negative energy transfer between −16 and −9 cm^{-1} (see Figure 7c, inset). On increasing the temperature from 15 to 30 K, these transitions shift from −13.58(2) cm^{-1} and −11.42(2) cm^{-1} to −12.98(3) cm^{-1} and −10.87(2) cm^{-1}, respectively. A weak feature grows in intensity with increasing temperature near the experimental cutoff of +12 cm^{-1}. Since the spectral bandwidths were near the instrument limits, we investigated this compound with MARS at 1.86 K. In addition to resolving the shoulder at 2.1 cm^{-1}, additional peaks at +11.78(1) cm^{-1} and +13.80(1) cm^{-1} energy transfers are clearly observed. The relative intensities of the inelastic transitions from low to high positive energy transfer in the MARS spectra collected at 1.86 K of NaMgV are approximately 6.7:1:5.1.

At 1.5 K, the INS spectrum of Na_3V displays two intense energy transfer peaks at ∼5.3 and ∼9.2 cm^{-1} (Figure 7b). These bands decrease in intensity with increasing temperature, and a new band at lower energies appears at ∼3.9 cm^{-1}.

The multiple sets of peaks seen in the low-temperature absorption spectra of K_3V are also observed in the INS spectra shown in Figure 7a. The spectrum collected at 1.5 K on FOCUS is more structured than for the other compounds with at least four resolved peaks and a broad shoulder from 7 to 8 cm^{-1}. These transitions decrease in intensity with increasing temperature to 30 K, and two broad transitions appear at lower energy transfers. The

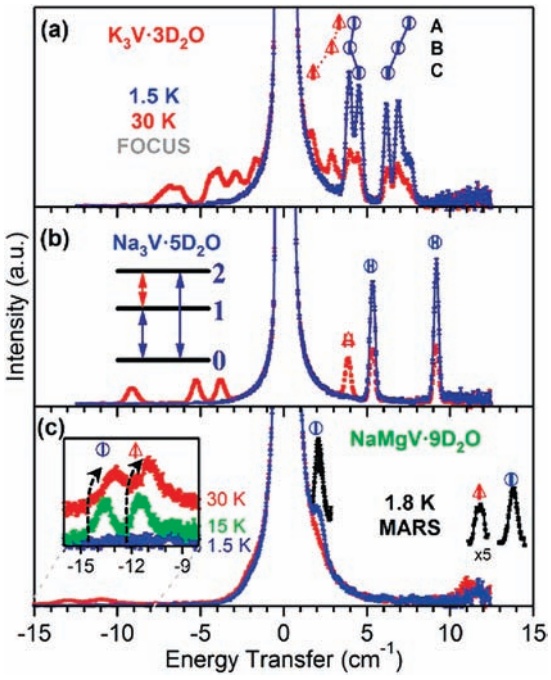

Figure 7. The 1.5 K (blue) and 30 K (red) INS spectra collected between ±15 cm^{-1} energy transfers on FOCUS (0.36 cm^{-1} spectral resolution) of fully deuterated (a) K_3V, (b) Na_3V, and (c) NaMgV. (c, inset) Variable-temperature INS spectra of NaMgV are shown in the region between −16 and −9 cm^{-1}. High-resolution INS spectra were collected on MARS at 1.86 K and 0.18 cm^{-1} spectral resolution for NaMgV (offset black lines, c). The symbols above the peaks are from the energy splittings of the BG lines given from the spectral deconvolution of the electronic absorption spectra shown in Figure 5 and given in Table 4. The circles in the spectra correspond to the expected energies of the transitions from the ground state, **0**, to the first two excited states, **1** and **2**, as shown in the inset of b. The triangles correspond to the **1** → **2** or "hot" transition.

intensity at negative energy transfer increases with increasing temperature; however, the large line widths of these peaks occlude any information regarding ZFSs in this region. The strong, resolved features at 1.5 K in the FOCUS spectra narrowed when collected at higher spectral resolution on MARS, indicating that they are instrument-broadened in the FOCUS spectrum. The INS spectra collected from 3.5 to 8 cm^{-1} energy transfer at higher spectral resolution with MARS and at 1.6 K are shown in Figure 8. The broad shoulder at high energy transfer is now resolved in the high-resolution INS spectra. In the 0.05 cm^{-1} resolution spectrum, this shoulder reveals what appears to be four overlapping transitions between 7 and 8 cm^{-1}. This region of the spectrum was deconvoluted with four Gaussian bands, and the individual peaks are labeled with Roman numerals in Figure 8. At lower energy transfer, the 0.10 cm^{-1} resolution INS spectrum reveals a broad shoulder at 4.34 cm^{-1}.

The transitions detected by INS spectroscopy can only come from transitions within the ground-state electronic structure of the V^{3+} ion. The ZFS's observed by INS spectroscopy were thus deconvoluted and compared to the splittings obtained by absorption spectroscopy given in Table 4.

5.3. Hamiltonian Calculations. Figure 9 shows the energies of the three lowest-energy spinor levels of the $^3T_{1g}$ ground term as a function of the splitting parameters Δ_{ax} and $|\Delta_{rh}|$ with $A\lambda = 80$ cm^{-1} calculated from eq 1. The states are labeled in order of ascending eigenvalues beginning with **0**, as shown in Figure 2. When $\Delta_{rh} = 0$ and Δ_{ax}^{+}

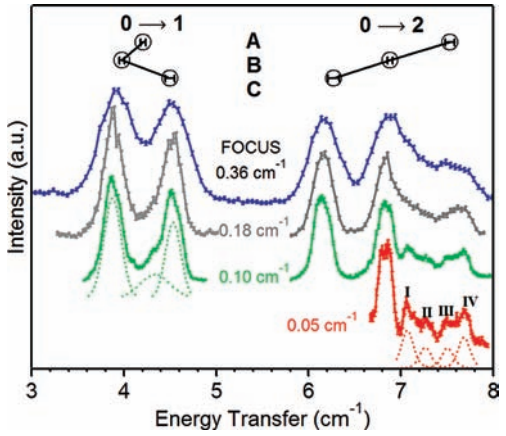

Figure 8. INS spectra collected at 1.6 K of fully deuterated K_3V with varying spectral resolution. Resolutions are given in the figure. Three sites are resolved for both the **0**→**1** and **0**→**2** transitions at high resolution with the MARS spectrometer. Additional features were resolved between a 7 and 8 cm^{-1} energy transfer when collected at 0.05 cm^{-1} spectral resolution. These features were deconvoluted with four individual Gaussian band shapes, which are shown in the figure and labeled with Roman numerals.

$\gg A\lambda$, level **0** is nondegenerate and levels **1** and **2** are degenerate. Under this scenario, the splitting of the states correlates directly with the $S = 1$ spin-Hamiltonian parameter, D, as given by eq 2. From Figure 9a, we see that, when Δ_{ax}^{+} is small compared to $A\lambda$, D increases linearly with Δ_{ax}^{+}; when Δ_{ax}^{+} is large compared to $A\lambda$, D diminishes with inverse proportion to Δ_{ax}^{+}, in accordance with expectations based upon perturbation theory, as given by eq 3a. The parameter D reaches a maximum for $\Delta_{ax}^{+} \approx A\lambda$. When $|\Delta_{ax}^{-}| \gg A\lambda$, the two lowest-lying spinors, that is, **0**,**1** and **2**,**3**, are both doubly degenerate. Figure 9a displays the splitting between the two states as a function of Δ_{ax}^{-}. This value approaches $A\lambda$ when $|\Delta_{ax}^{-}| \gg 0$.

In Figure 9b, the energies of states **1** and **2** relative to state **0** are plotted as a function of $|\Delta_{rh}|$ for values of $|\Delta_{ax}| =$ 600, 1000, and 1400 cm^{-1} and $A\lambda = 80$ cm^{-1}. When $\Delta_{ax} \gg 0$, the energy difference between **1** and **2** is equal to $2|E|$, where E is the rhombic spin-Hamiltonian parameter given in eq 2. For small values of $|\Delta_{rh}|$, the states split linearly with $|\Delta_{rh}|$ in accordance with eq 3b. At larger values of $|\Delta_{rh}|$, the asymmetry in the splitting behavior of states **1** and **2** is significant. This is seen clearly in Figure 9c, where the derivatives of the curves in Figure 9b are plotted for the different values of Δ_{ax} as a function of Δ_{rh} (see the Supporting Information, Figure S6). We term this effect anisotropic E-strain, which has a profound effect on the INS band profiles, particularly for K_3V, as we shall show below.

When $\Delta_{ax} \ll 0$ and $|\Delta_{rh}| \gg A\lambda$, the energy difference between states **0** and **1** is small and corresponds to $2|E|$, in contrast to the case when Δ_{ax}^{+} and the smallest splitting is between states **1** and **2** (see Figure 9b). States **0** and **1** split linearly with increasing $|\Delta_{rh}|$, but as $|\Delta_{rh}| \gg A\lambda$, the energy of **1** levels off and becomes parallel to **0**. The energy difference between **2** and **3** approaches $2|\Delta_{rh}|$ when $|\Delta_{ax}^{-}|$ is large, as shown schematically in Figure 2. Figure 9c shows the relative rates of change of the energies of **1** and **2** with respect to $|\Delta_{rh}|$ when $\Delta_{ax} = -600, -1000,$ and -1400 cm^{-1}. The same trend is observed when $\Delta_{ax} \ll 0$ as when $\Delta_{ax} \gg 0$. Specifically, the relative change of **2** is always more sensitive to changes in Δ_{rh} compared to state **1** independent of the sign of Δ_{ax}.

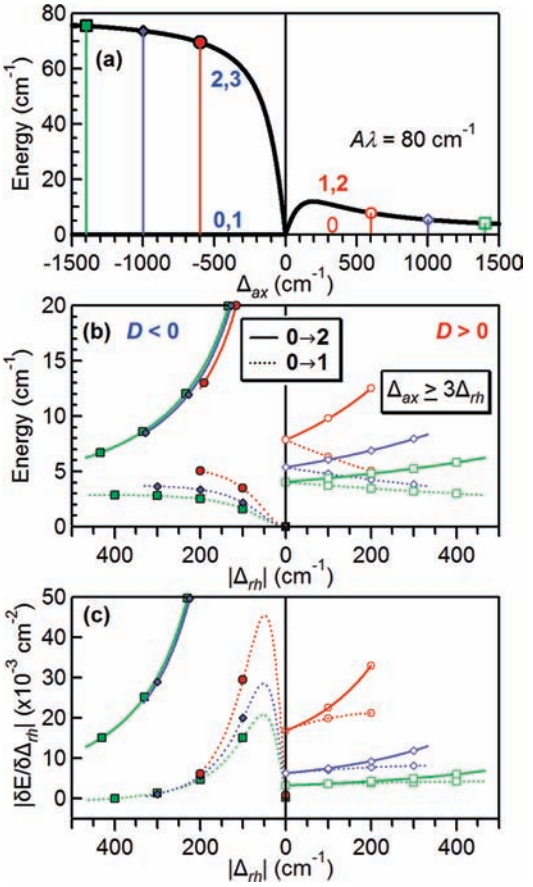

Figure 9. (a) Calculated energies using eq 1 of the two lowest-energy spinors when $A\lambda = 80$ cm^{-1} and $\Delta_{rh} = 0$ as a function of Δ_{ax}. (b) Calculated splitting behavior of the doubly degenerate spinors as a function of Δ_{rh} when $A\lambda = 80$ cm^{-1} for $|\Delta_{ax}| = 600$ (○), 1000 (◇), and 1400 (□) cm^{-1} as shown in a. Level **3** increases dramatically with increasing $|\Delta_{rh}|$ and is quickly absorbed into the higher-energy orbital singlet when $|\Delta_{ax}^{-}| \gg |\Delta_{rh}| \gg A\lambda$. The **0**→**2** and **0**→**1** transition energies are shown as solid and dashed lines, respectively. (c) Calculated partial derivatives (absolute values) of the **0**→**2** and **0**→**1** energies as a function of $|\Delta_{rh}|$ at the same Δ_{ax} values as in b. The upper limit on the values of $|\Delta_{rh}|$ for the energies of **1** and **2** in b and c is $\Delta_{ax}/3$ in accordance with the restrictions of eqs 3c and 4c.

6. Discussion

6.1. Absorption Spectroscopy. The spin-allowed and spin-forbidden d−d transitions were assigned above from the electronic absorption spectra shown in Figure 3 and Figures 4 and 5, respectively. The Racah (B_c, C_c) and octahedral splitting (10Dq) parameters of the $[V(ox)_3]^{3-}$ chromophores are determined by the energies of the spin-forbidden $^1T_{2g}(D)$ and spin-allowed $^3T_{2g}(F)$ and $^3T_{1g}(P)$ transitions. The energy of the $^1T_{2g}(D)$ transition is taken from the low-temperature absorption spectra shown in Figure 4. It spans from ~9400 to 9650 cm^{-1} depending on the lattice. The energies of the spin-allowed transitions are taken from the room-temperature solution spectrum of K_3V shown in Figure 3a with $^3T_{1g}(F) \rightarrow {}^3T_{2g}(F) =$ 16 550 cm^{-1} and $^3T_{1g}(F) \rightarrow {}^3T_{1g}(P) =$ 23 650 cm^{-1}. Fitting these energies to the theoretical equations derived from the Tanabe−Sugano energy matrices[45] (see Appendix B) yield ligand-field parameters of 10Dq = 17 733 cm^{-1}, $B_c =$

(45) Sugano, S.; Tanabe, Y.; Kamimura, H. *Multiplets of Transition-Metal Ions in Crystals*. Academic: New York, 1970.

552.2 cm^{-1}, and $C_c = 3007\ cm^{-1}$. These values are included in Table 2. The nephelauxetic ratio is $\eta = B_c/B_o = 0.62$ (free ion value, $B_o = 886\ cm^{-1}$, $C_o/B_o = 4.0$).[45,46] The increase in C_c/B_c compared to the free-ion ratio for coordination compounds has been shown previously both by experiment[47] and by theory.[48] Assuming that η is also a reasonable estimate for the analogous orbital reduction factor, k,[49] we calculate the spin−orbit coupling constant of the strong-field $^3T_{1g}$ ground term as $\lambda = k\zeta_o/2S = 65\ cm^{-1}$, where ζ_o is the free-ion spin−orbit coupling constant equal to 210 cm^{-1}.[50] When the Dq and B_c values are used, the mixing parameter of the two $^3T_{1g}$ strong-field terms yields a value of $A = 1.25$.[50] This mixing parameter scales the effective term spin−orbit coupling constant of the intermediate-field ground state to give $A\lambda \approx 80\ cm^{-1}$. This value will be used throughout the paper when calculating ZFSs.[51]

For comparison, the ligand-field parameters have been deduced in the same way from the transition energies of V^{3+} in the Al_2O_3 lattice (Table 2).[25] As expected, the 10Dq and B_c values are larger in the corundum lattice. The calculated A value, as a result of both parameters increasing, is the same value as for the trisoxalate ligand field. Due to the larger value of η, and our assumption that $\eta \approx k$, the term spin−orbit coupling constant is ∼13% larger for the Al_2O_3:V compound, $A\lambda = 90\ cm^{-1}$.

Though the polar angle of the chromophore in our compounds would suggest a trigonal compression and thus a positive diagonal trigonal field, the splitting is reversed on account of the acute bite angles of the oxalate ligands expressed by a large deviation in the twist angle, $\varphi < \varphi_{cube} = 60°$ (see Table 1).[32,38] However, extension of our treatment of the trisoxalate ligand field to include trigonal crystal field parameters, as was done for Al_2O_3:V,[26,52,53] is not possible due to (1) the inability to resolve the $^3T_1(P)$ transition in the $E\perp D_3$ spectrum and (2) the absence of enough physical observables to justify the inclusion of two additional parameters. Therefore, we cannot include such a treatment of $[V(ox)_3]^{3-}$ here.

6.2. INS Spectroscopy and Ground-State Electronic Structure. The INS spectra presented in Figure 7 provide a direct measure of the transition energies from the lowest-lying spinor levels within the $^3T_{1g}$ ground term. The transition energies observed by INS spectroscopy agree with the ΔE values from the high-resolution absorption spectra of the NIR and BG lines shown in Figures 4 and 5 to within ∼1%. This agreement provides important structural information since the spectra were collected on crystals grown from H_2O and D_2O solutions for absorption and INS spectroscopies, respectively. It thus follows that the active structural perturbations in the trisoxalate compounds that give rise to the observed axial and rhombic ZFSs are similar for the perprotonated and perdeuterated lattices at low temperatures (see Table 4). Previous studies on the axially distorted V^{3+}-alums by high-field, high-frequency EPR spectroscopy also report ground-state ZFSs with similar relative deviations of ∼2% between $(H_2O)_6$ and $(D_2O)_6$.[54,55] This result is interesting because in the V^{3+}-alums the water molecules are directly coordinated to the metal center, whereas in the trisoxalate compounds the waters are perturbing the V^{3+} ion indirectly through secondary interactions.

Table 5. Ground-State ZFS Values Determined for the $[V(ox)_3]^{3-}$ Compounds Using eq 2 and the ΔE Values Given in Table 4[a]

lattice		D (cm^{-1})	$\lvert E\rvert$ (cm^{-1})	$\lvert E\rvert/D$	technique	reference
Al_2O_3		+8.34(3)	0	0	FT-abs	this work
		8.29	0	0	HF-EPR	63
		8.25	0	0	far-IR abs	64
K_3V	**A**	+5.87(6)	1.66(3)	0.28		
	B	+5.43(5)	1.45(4)	0.26	FT-abs[b]	this work
	C	+5.39(8)	0.89(5)	0.17		
	A	+6.0(2)	1.67(7)	0.28		
	B	+5.36(1)	1.48(1)	0.28	INS[c]	this work
	C	+5.34(1)	0.81(1)	0.15		
		+3.84	0	0	magn. susc.	6
Na_3V		+7.2(3)	1.9(2)	0.26	FT-abs[b]	this work
		+7.26(1)	1.92(1)	0.26	INS[c]	
NaMgV		−12.72(5)	0.97(5)	−0.08	FT-abs[b]	this work
		−12.75(1)	1.05(1)	−0.08	INS[c]	
NaMgAl:V		−9.78(5)	1.50(4)	−0.15	FT-abs	this work
$V(acac)_3$		+7.47	1.92	0.26	HF-EPR	57

[a] ZFS values of other selected trigonally-distorted V^{3+} compounds are given for comparison. The sign of E cannot be deduced from the spectroscopic measurements. [b] Single crystals grown from H_2O solutions. [c] Powders obtained from D_2O solutions.

Analysis of the ΔE values of the BG line and INS spectra using the spin Hamiltonian yields D and $|E|$ values shown in Table 5. The D values for Na_3V and for all sites of K_3V are positive with $|E/D|$ ratios between 15 and 28%. The axial ZFS parameter of NaMgV and NaMgAl:V is negative with D values of −12.75 and −9.78 cm^{-1}, respectively, and smaller ratios of $|E/D|$ of ∼8−15%. The temperature dependence of the INS spectra, shown in Figure 7, provides the key experimental confirmation of the sign of D. The absolute intensity of the lowest-energy transition will increase (decrease) with increasing temperature when D is positive (negative). For deuterated K_3V and Na_3V, the lowest-energy transition appears with increasing temperature, confirming a positive sign for D. The INS spectra of deuterated NaMgV on the other hand displays a transition at ∼2 cm^{-1} at 1.6 K that immediately decreases in intensity with increasing temperature and is thus consistent with a negative sign for D. The sign of D for all previously studied V(III) hexavalent-oxo compounds[21−23,54,56] has always been positive with small or

(46) Brorson, M.; Shäffer, C. E. *Inorg. Chem.* **1988**, *27*, 2522–2530.
(47) Ferguson, J.; Wood, D. L. *Aust. J. Chem.* **1970**, *23*, 861–871.
(48) Atanasov, M.; Daul, C. A.; Rauzy, C. *Chem. Phys. Lett.* **2003**, *367*, 737–746.
(49) Figgis, B. N.; Hitchman, M. A. *Ligand Field Theory and Its Applications*; Wiley-VCH: New York, 2000.
(50) Mabbs, F. E.; Machin, D. J. *Magnetism and Transition Metal Complexes*; Chapman and Hall: London, 1973.
(51) In our ligand field analysis, the C_c value is determined by the energy of the $^1T_{2g}(D)$ transition. Changing this energy to 9400 cm^{-1} as for K_3V and Na_3V changes this value to $C_c = 2912\ cm^{-1}$; however, the C_c parameter does not affect the mixing parameter, A.
(52) Macfarlane, R. M. *J. Chem. Phys.* **1964**, *40*, 373–377.
(53) Rahman, H. U.; Runciman, W. A. *J. Phys. C: Solid. State Phys.* **1971**, *4*, 1576–1590.
(54) Tregenna-Piggott, P. L. W.; Spichiger, D.; Carver, G.; Frey, B.; Meier, R.; Weihe, H.; Cowan, J. A.; McIntyre, G. J.; Zahn, G.; Barra, A. L. *Inorg. Chem.* **2004**, *43*, 8049–8060.
(55) Tregenna-Piggott, P. L. W.; Weihe, H.; Bendix, J.; Barra, A. L.; Güdel, H. U. *Inorg. Chem.* **1999**, *38*, 5928–5829.
(56) Dingle, R.; McCarthy, P. J.; Ballhausen, C. J. *J. Chem. Phys.* **1969**, *50*, 1957–1962.

negligible rhombic ZFS with the only exception being $V(acac)_3$, a tris-bidentate compound with $D = 7.47\ cm^{-1}$, and a comparatively large $|E| = 1.916\ cm^{-1}$.[57]

As a consequence of the low symmetry of the V^{3+} ion in hydrated trisoxalate lattices and the appreciable rhombic component determined above, we have estimated the splittings of the $^3T_{1g}$ ground term using eq 1 with the effective spin−orbit coupling constant of $A\lambda = 80\ cm^{-1}$ (vide supra). The ΔE values for the two lowest-lying excited states of the BG lines were used in the fitting procedure. The magnitudes of the Δ_{ax} and Δ_{rh} splitting parameters are given in Table 6. The calculated $|\Delta_{ax}|$ values are large, but likewise change in sign as above. The change in sign of the Δ_{ax} parameter means that the $^3T_{1g}$ ground term splits such that the $^3A_2$ term is the ground term for K_3V and Na_3V, whereas for NaMgAl:V and NaMgV in the absence of Δ_{rh} it is the ^3E term (see Figure 2). The effect of the additional Δ_{rh} splitting on the ground-state electronic structures for both scenarios is shown in Figure 9b. The calculated axial ZFS parameter from the splitting of the three spinors predicts that for $|\Delta_{rh}|$ values less than $|\Delta_{ax}|/3$ only positive (negative) D values can result from Δ_{ax} values that are positive (negative) and large.

Atanasov and co-workers showed that for planar bidentate ligands the orientations of the ligand π orbitals are geometrically fixed.[32] This results in an isotropic contribution to the axial splitting from π bonding. Comparison of the various crystallographic parameters in Table 1 reveals that the torsion angles of the oxalate ligands display the largest deviations from their average value for NaMgAl among the compounds studied with $\sigma(\bar{\gamma}) = 4.96°$. For linear ligators, the expected contribution from π bonding to the overall axial splitting is small. Nonlinear ligators, however, can influence both the magnitude and sign of Δ_{ax}.[32,37,58] In the present case, the orientation of the in-plane and out-of-plane π orbitals is thought to be correlated to the spatial arrangement of the water molecules participating in the H bonding.[32] The small deviation on the mean V−O−C bond angle of NaMgAl of ∼0.4° (see Table 1) may also contribute to a perturbed electronic structure by misaligning the σ-bonding orbitals of the oxygens (misdirected valency[33−35]). We therefore hypothesize that the dominant factor responsible for the additional negative Δ_{ax} splitting for NaMgV and NaMgAl:V, and subsequent negative D, results primarily from the anisotropic ligand fields of the $[M(ox)_3]^{3-}$ structure, induced by interactions from the second coordination sphere.[59]

In contrast, the positive D values for K_3V and Na_3V are unusual on the basis of the expectation of a negative value for the $[V(ox)_3]^{3-}$ chromophore in the absence of a rhombic ligand field, as discussed in section 6.1. The bending of the trigonal axes in these two compounds is large and suggests that this distortion coordinate may be responsible for effectively changing the sign of the ground-state splitting to positive Δ_{ax} values by increasing the magnitude of $|\Delta_{rh}|$ such that it becomes larger than the inherent negative trigonal field. These various effects are currently being studied within the framework of the angular overlap model and will be presented elsewhere.

Table 6. Estimated Axial and Rhombic Splitting Parameters[a] of the $^3T_{1g}$ Ground Term Obtained by Fitting the ΔE Values for Al_2O_3:V and the Various Hydrated $[V(ox)_3]^{3-}$ Compounds Using the LF Hamiltonian (eq 1) with a Constant Spin-Orbit Coupling Constant of $A\lambda = 80\ cm^{-1}$

lattice		$A\lambda$	Δ_{ax}	$\lvert\Delta_{rh}\rvert$	$\lvert\Delta_{rh}\rvert/\Delta_{ax}$
Al_2O_3:V		90	734	0	0.00
K_3V	**A**	80	961	231	0.24
	B	80	1052	242	0.23
	C	80	1020	144	0.14
Na_3V		80	731	160	0.22
NaMgV		80	−1915	209	−0.11
NaMgAl:V		80	−1236	248	−0.20

[a] The ratio of the rhombic and axial splittings deviates by at most 13% over the range of $A\lambda$ values from 60 to 120 cm^{-1}. Energies are given in cm^{-1}.

The INS spectra shown in Figure 7 display an interesting temperature dependence for the different compounds. The transition energies of K_3V and Na_3V do not shift below 30 K. In contrast, the INS spectra of NaMgV show a synchronized red shift of the resolved **0** → **2** and **1** → **2** transitions upon warming, shown in the inset of Figure 7c. This result is curious since the ΔE values from the temperature dependence of the electronic origins of perprotonated NaMgV are constant over this temperature range (see Figure S5, Supporting Information). Riesen and Hughes studied the persistent hole-burning mechanism of the R_1 line of NaMgAl:Cr and showed that the hole-burning efficiency can be greatly enhanced by partial deuteration of the lattice, which they attribute to 180° flips of crystalline water molecules.[17] The temperature dependence of the spontaneous hole-filling provided experimental evidence of an elaborate H-bonding network, with three distinct types of H bonding being active in the NaMgAl lattice.[18] We agree that the flipping motion of the free water molecules is active in NaMgV, but we argue that the apparent decrease of the axial ZFS parameter must arise from changes in the axial and rhombic ligand fields with increasing temperature in accordance with eq 4a. Thus, we assign this phenomenon to differences in the temperature-dependent dynamics of the D bonding as compared to the H bonding with the oxalate ligands of the $[V(ox)_3]^{3-}$ complex.

6.3. Intraconfigurational Spin-Forbidden Transitions. Now that we have identified the sign and magnitudes of the ground-state ZFS parameters, we will discuss the transitions to the narrow absorption features in Figures 4 and 5. The NIR and BG lines were reported previously for NaMgAl:V by Piper and Carlin over 40 years ago; however, there was no mention of any additional splitting of these lines, most probably due to a combination of instrument-limited spectral resolution, a high collection temperature of 77 K where all of the states are populated, and a high concentration of V^{3+} in the crystal.[10] The inhomogeneous line widths, Γ_{inh}, in the studied compounds provide valuable information regarding the site homogeneity of the chromophores. Even in K_3V, where there are multiple sites, $\bar{\Gamma}_{inh}$ of the NIR lines are $< 1.5\ cm^{-1}$. For all compounds studied, the Γ_{inh} of the NIR lines is narrower than that of the corresponding BG lines. This can

(57) Krzystek, J.; Fiedler, A. T.; Sokol, J. J.; Ozarowski, A.; Zvyagin, S. A.; Brunold, T. C.; Long, J. R.; Brunel, L.-C.; Telser, J. *Inorg. Chem.* **2004**, *43*, 5645–5658.
(58) Daul, C.; Goursot, A. *Inorg. Chem.* **1985**, *24*, 3554–3558.
(59) Reinen, D.; Atanasov, M.; Lee, S.-L. *Coord. Chem. Rev.* **1998**, *175*, 91–158.

be explained by configuration interaction with a higher-energy $^1A_{1g}$ (^1S, e_g^2 strong-field configuration) state giving rise to a nonvanishing Dq dependence on the energy of the $^1A_{1g}$(G) BG lines compared to the NIR lines (see Appendix B).[52,56,61]

The observed electronic origin in the near-IR shown in Figure 4 originates from one of the five possible spin-forbidden transitions expected from V^{3+} in rhombic site symmetry. An electronic absorption feature is observed at 9748 cm^{-1} for Al_2O_3:V and has been assigned to the ^1E component from the trigonally split $^1T_{2g}$ excited state on the basis of polarized Zeeman and luminescence spectroscopies.[23−26] This state is also the emissive state in NaMgAl:V at cryogenic temperatures.[60] On the basis of an analysis of the ground-state splitting using eq 1 shown in Table 6, we demonstrated a change in sign of the Δ_{ax} splitting parameter for NaMgAl:V and NaMgV compared to the other $[V(ox)_3]^{3-}$ compounds and Al_2O_3:V. However, the expected splitting of the $^1T_{2g}$ term into the $^1A_1$ and ^1E states in D_3 point symmetry may not necessarily correlate with the splitting of the $^3T_{1g}$ ground term due to the low symmetry of the complex.[28] The spin-forbidden bands exhibit a larger degree of polarization than expected for the low site symmetry of these compounds. It thus appears that the rhombic distortion does not noticeably affect the dipole selection rules from inherent molecular symmetry of the tris-bidentate coordination in at least the highest symmetry lattices, which are NaMgAl:V and NaMgV. Using the electric dipole selection rules from the D_3 double group defined in eq 6, we can compare the spectra shown in Figures 4 and 5 and attempt to assign the most likely $^1\Gamma(^1T_{2g})$ component responsible for the NIR lines between the different compounds.

$$\Gamma_1 = A_1 = |0,0\rangle, |+\tilde{1}, +1\rangle \quad (6a)$$

$$\Gamma_2 = A_2 = |-\tilde{1}, -1\rangle \quad (6b)$$

$$\Gamma_3 = E = |0, \pm 1\rangle, |\pm \tilde{1}, 0\rangle, |\pm \tilde{1}, \mp 1\rangle \quad (6c)$$

$$\Gamma_{1(2)} \leftrightarrow \Gamma_{1(2)} \text{ (forbidden)} \quad (6d)$$

$$\Gamma_{1(2)} \leftrightarrow \Gamma_{2(1)} \text{ (z)} \quad (6e)$$

$$\Gamma_{1(2)} \leftrightarrow \Gamma_3 \text{ (xy)} \quad (6f)$$

$$\Gamma_3 \leftrightarrow \Gamma_3 \text{ (xyz)} \quad (6g)$$

The electric dipole selection rules are defined using both irreducible representations of the D_3 double group and ground-state wave functions defined by the ligand field Hamiltonian from eq 1.[50] The Γ_2 state originating from the ^3E multiplet is absorbed by one of the higher-lying orbital singlets of the $^3T_{1g}$ ground term when $|\Delta_{ax}^-|$ and $|\Delta_{rh}|$ are large, and transitions from this state can thus be ignored (see Figure 2).

The BG line originates from the totally symmetric $^1A_{1g}$ (Γ_1) excited state in O_h symmetry and is therefore an ideal transition to determine the agreement between dipole selection rules and polarized absorption spectra of Figure 5. The highest-symmetry lattices in this study are NaMgAl:V and NaMgV, for which the orientation of the pseudotrigonal axis of the trisoxalate chromophore in NaMgAl is within 2° of the *c* axis.[18] For NaMgAl:V and NaMgV, we showed above that *D* is negative and $M_S = \pm 1 < M_S = 0$. However, all spinors of the ground state have Γ_3 parentage, and we would expect to see similar polarizations for the individual components of the NIR and BG lines. The BG line shows that all of the bands are observed only in the *xy* spectrum, in excellent agreement with the eq 6f. The low intensity of the feature at ~20 455 cm^{-1} originating from the highest-lying component of the ground-state triplet (**2**) is simply due to Boltzmann statistics. Previous analysis of the temperature dependence of the BG line for NaMgAl:V showed that the relative oscillator strengths between the three lines was 0.83:0.60:1 in order of increasing transition energy.[60] The three components of the NIR lines of NaMgAl:V and NaMgV are observed in both *xy* and *z* polarized spectra, which requires the Γ_3 (^1E) parentage to be responsible for the NIR lines. The splitting diagram and expected polarizations of the NIR and BG lines of the $[V(ox)_3]^{3-}$ complex in NaMgAl and NaMgV lattices are shown on the left-hand side of Figure 2.

The ordering of the ground-state M_S levels of K_3V and Na_3V is $M_S = 0 < M_S = \pm 1$ ($\Gamma_1 < \Gamma_3$). The expected polarization of the BG line for positive *D* is thus *xy*, *xy*, *z* with increasing energy. The observed polarizations for K_3V and Na_3V do not agree with these expectations. In addition to this difference, there are other violations between the observed and expected polarizations of the NIR and BG lines that suggest the low-symmetry distortions of the chromophore in the K_3V and Na_3V lattices are stronger than in the NaMgAl:V and NaMgV lattices. On the basis of these variations in the polarized spectra, we cannot assign with confidence the $^1T_{2g}$ component responsible for the NIR lines of K_3V and Na_3V.

As a result of the different sign of the ground-state axial ZFS and crystallographic distortions, the observed polarizations of the NIR and BG lines appear quite different for all of the compounds. The dominant factor for the observed violations of the D_3 selection rules is attributed to differences in the bending angle, β (Table 1). In NaMgAl, this angle is 179.5°, which is very close to the ideal value of 180° in D_3 symmetry, while for Na_3Cr (178.8°) and K_3V (176.5°), substantial deviations from D_3 symmetry are observed. The assignments given for the NIR lines for all of the compounds are tentative and currently being investigated by full ligand field calculations using the angular overlap model and Zeeman spectra.

6.4. Crystallographic Phase Transition of $K_3V(ox)_3 \cdot 3H_2O$. The observation of multiple transitions and the interesting temperature dependence of K_3V shown in the electronic absorption (Figures 4−6) and INS spectra (Figures 7,8)

(60) Kittilstved, K. R.; Hauser, A. *J. Lumin.* [Online] DOI: 10.1016/j.jlumin.2009.1002.1021.

(61) Tanabe, Y.; Sugano, S. *J. Phys. Soc. Jpn.* **1954**, *9*, 753–766.

can only be explained by a low-temperature crystallographic phase transition. On the basis of the similarity between the polarization ratios of the different sets in the NIR and BG lines, it appears that the molecular symmetry of each site is in a similar orientation with respect to one another in the low-temperature phase (LTP). The oscillator strengths of the NIR lines in Figure 4a for K_3V are $1.21(2) \times 10^{-8}$, $1.26(3) \times 10^{-8}$, and $1.11(4) \times 10^{-8}$ for sites **A**, **B**, and **C**, respectively, thus supporting a scenario where the V^{3+} site splits equally into three sites in the LTP.

The instrument resolution with FOCUS was insufficient to resolve the expected three sets of transitions that we were able to easily resolve in the absorption spectra. The INS spectra appear to show only two unique V^{3+} sites in the LTP in Figure 7. However, since the line widths are relatively large for the INS spectra collected at 0.36 cm^{-1}, we cannot exclude the possibility that the expected **0** → **1** transition from site **A** is occluded by the peaks associated with sites **B** and **C** between 3.5 and 5 cm^{-1} in Figure 7. The INS spectrum collected at 0.10 cm^{-1} resolution in the region from 3.5 to 5 cm^{-1} indeed reveals a shoulder between the two intense peaks centered at 4.34(6) cm^{-1} of similar breadth to the feature at 7.67(2) cm^{-1} (see Figure 8). We assign this shoulder to the **0** → **1** transition of site **A**. The broad shoulder between 7 and 8 cm^{-1} in the INS spectra shown in Figure 7 is in the energy region where the **0** → **2** transition from set **A** is expected to appear on the basis of the ΔE values of the NIR and BG lines (see Table 4). INS spectra collected at a superior instrument resolution on MARS of this shoulder clearly resolve a transition at 7.67(2) cm^{-1}.

INS spectra collected at an even higher resolution of 0.05 cm^{-1} further resolve more transitions over this shoulder that are labeled with Roman numerals in Figure 8 that we assign as additional minority sites. Sites **A** and **B** have large rhombic contributions to the ground-state splitting of the three sites by absorption spectroscopy (Table 6). When coupled to the results from the calculations presented in Figure 9, we gain a better understanding about the breadth of this transition in the INS spectra and additional subsets originating from sites **A** and **B**. We show in Figure 9 that the energies of the two lowest-lying levels are very sensitive to the axial and rhombic crystal fields. Furthermore, when the rhombic field becomes comparable to the axial field, one cannot ignore the anisotropic *E*-strain in the ground-state electronic structure. The results presented in Figure 9b,c provide us with the theoretical basis to rationalize the observations in the INS spectra of K_3V, especially of sites **A** and **B** with the largest $|E|/D$ ratios. We propose that the anisotropic *E*-strain of specifically state **2** of sites **A** and **B** shown generically in Figure 9c explains both the larger width and additional sites for the **0** → **2** transitions in the INS spectra shown in Figure 8.

Our spectroscopic results are consistent with a scenario with three unique $[V(ox)_3]^{3-}$ sites in the LTP. If we assume the LTP to be a subgroup of the high-temperature phase (HTP = $P2_1/c$, $Z_{HTP} = 4$), then there is a possibility of obtaining a tripling of the lattice along the *b* axis while staying in the $P2_1/c$ setting with $Z_{LTP} = 12$. Corresponding low-temperature crystallographic studies are currently underway to investigate the nature of the suspected LTP.

7. Conclusions

Axial and rhombic ZFSs of the ground state of V^{3+} in various hydrated trisoxalate compounds have been observed at low temperatures by Fourier transform absorption and INS spectroscopies. Evidence of a crystallographic phase transition in K_3V has been presented by both spectroscopies.

Analysis of the ZFSs revealed that the magnitude *and* sign of the spin-Hamiltonian parameters differ greatly for the same $[V(ox)_3]^{3-}$ molecular complex depending on the crystalline lattice. We have provided crystallographic evidence that the H bonding between the oxalate ligands and water molecules in the second coordination sphere is responsible for this phenomenon in the V^{3+} ground state. These interactions create anisotropic ligand fields that have been identified by (1) variations in the V−O bond lengths and (2) variations in the O−V−O bite angles, (3) removal of the mirror plane or C_2 symmetry of the oxalate ligands defined by a nonzero torsion angle, and (4) a bending of the trigonal axes from 180° in the D_3 symmetry.

Estimates of Δ_{ax} using eq 1 resulted in negative values (^3E ground term) for NaMgAl:V and NaMgV and positive values ($^3A_2$ ground term) for K_3V and Na_3V. We propose that the change in sign originates from bending of the trigonal axes of the chromophore and anisotropic π-bonding contributions to the axial field due to the nonplanarity of the oxalate ligands. We have provided experimental evidence that the ground-state electronic structure cannot be described by a simple trigonally distorted octahedron for V^{3+} in trisoxalate lattices when noninnocent counterions or waters of hydration are present. These results provide the potential ability to design oxalate or similar ligand-based mixed-valence magnetic materials with desirable and controllable properties.

We shall proceed to analyze the H-bonding, in particular, in NaMgAl:V and NaMgV, in more detail by means of low-temperature crystallographic techniques and to discuss the polarized single-crystal absorption spectra in the region of the spin-forbidden transitions in conjunction with low-temperature Zeeman spectra.

Acknowledgment. We thank J.-N. Chotard and N. Penin for recording the X-ray powder diffraction patterns of Na_3V and NaMgV and C. Bésnard for interpretation (all at Université de Genève). This work was financially supported by the Swiss National Science Foundation (Grant No. 200020-115867). The INS experiments were performed at the Swiss spallation neutron source SINQ, Paul Scherrer Institute, Villigen, Switzerland.

Supporting Information Available: Additional figures are given, including ORTEP representations of the various distortions of the $[M(ox)_3]^{3-}$ complex of K_3V and Na_3Cr; thermogravimetric analysis of K_3V, Na_3V, and NaMgV powders; comparison of experimental powder X-ray diffraction patterns for Na_3V and NaMgV with the simulated patterns of Na_3Cr[31] and NaMgAl,[18] respectively; temperature dependence of the BG line of NaMgV; a graphical step-by-step walkthrough to obtain the curves in Figure 9c from the curves in Figure 9b; and plots showing the agreement between the perturbation expressions

(eqs 4a and 4b) and calculated ground-state splittings using eq 1 when $|\Delta_{ax}^{-}| \gg |\Delta_{rh}| \gg A\lambda$. This material is available free of charge via the Internet at http://pubs.acs.org.

Appendix A. LF Hamiltonian matrix used to quantify the axial and rhombic orbital distortion parameters. Magnetic property analysis software, MagProp, was used to generate this Hamiltonian and fit the experimental energies of the two lowest excited states that were observed in the FT-absorption and INS spectra. The software is very versatile and can be used to import SQUID data (Quantum Design format), easily generate Hamiltonians, and simultaneously fit magnetic data and ligand-field energies to parameters defined by the user's input Hamiltonian and Zeeman matrices. The software was written by one of the authors (P.L.W.T.-P.) and is included free-of-charge with the DAVE software package.[43]

$$
\begin{array}{c|ccccccccc}
 & |\tilde{1},1\rangle & |\tilde{1},0\rangle & |\tilde{1},-1\rangle & |0,1\rangle & |0,0\rangle & |0,-1\rangle & |-\tilde{1},1\rangle & |-\tilde{1},0\rangle & |-\tilde{1},-1\rangle \\
\langle\tilde{1},1| & \frac{1}{3}\Delta_{ax}-A\lambda & 0 & 0 & 0 & -A\lambda & 0 & \Delta_{rh} & 0 & 0 \\
\langle\tilde{1},0| & 0 & \frac{1}{3}\Delta_{ax} & 0 & 0 & 0 & -A\lambda & 0 & \Delta_{rh} & 0 \\
\langle\tilde{1},-1| & 0 & 0 & \frac{1}{3}\Delta_{ax}+A\lambda & 0 & 0 & 0 & 0 & 0 & \Delta_{rh} \\
\langle 0,1| & 0 & 0 & 0 & \frac{-2}{3}\Delta_{ax} & 0 & 0 & 0 & -A\lambda & 0 \\
\langle 0,0| & -A\lambda & 0 & 0 & 0 & \frac{-2}{3}\Delta_{ax} & 0 & 0 & 0 & -A\lambda \\
\langle 0,-1| & 0 & -A\lambda & 0 & 0 & 0 & \frac{-2}{3}\Delta_{ax} & 0 & 0 & 0 \\
\langle -\tilde{1},1| & \Delta_{rh} & 0 & 0 & 0 & 0 & 0 & \frac{1}{3}\Delta_{ax}+A\lambda & 0 & 0 \\
\langle -\tilde{1},0| & 0 & \Delta_{rh} & 0 & -A\lambda & 0 & 0 & 0 & \frac{1}{3}\Delta_{ax} & 0 \\
\langle -\tilde{1},-1| & 0 & 0 & \Delta_{rh} & 0 & -A\lambda & 0 & 0 & 0 & \frac{1}{3}\Delta_{ax}-A\lambda
\end{array}
\qquad \text{(A1)}
$$

Appendix B. The calculated expressions for the energies of the $^1T_{2g}(D)$, $^3T_{2g}(F)$, $^1A_{1g}(G)$, and $^3T_{1g}(P)$ excited states are provided here. The ligand-field parameters (10Dq, B and C) were determined by a least-squares fitting of the full 45×45 ligand-field matrix for a d^2 ion in an octahedral field created with LigField[62] to the experimental energies given in Table 2 using MagProp.[43]

$$
\begin{aligned}
E(^1T_2(D)) &= B+\frac{1}{2}(4C+5^{1/2}[45B^2+36B\mathrm{Dq}+20\mathrm{Dq}^2]^{1/2}-[49B^2 \\
&\quad -20B\mathrm{Dq}+100D\mathrm{q}^2]^{1/2}) \qquad \text{(B1)}
\end{aligned}
$$

$$
\begin{aligned}
E(^3T_2(F)) &= \frac{1}{2}(-15B+10\mathrm{Dq}+5^{1/2}[45B^2+36B\mathrm{Dq}+20\mathrm{Dq}^2]^{1/2}) \qquad \text{(B2)}
\end{aligned}
$$

$$
E(^3T_1(P)) = 5^{1/2}[45B^2+36B\mathrm{Dq}+20\mathrm{Dq}^2]^{1/2} \qquad \text{(B3)}
$$

$$
\begin{aligned}
E(^1A_{1g}(G)) &= 5\mathrm{Dq}+\frac{1}{2}(19B+9C+5^{1/2}[45B^2+36B\mathrm{Dq}+20\mathrm{Dq}^2]^{1/2} \\
&\quad -5^{1/2}[20B^2+20BC+5C^2-16B\mathrm{Dq}-8C\mathrm{Dq}+80\mathrm{Dq}^2]^{1/2}) \qquad \text{(B4)}
\end{aligned}
$$

(62) Bendix, J. *Compr. Coord. Chem. II* **2004**, *2*, 673–676.
(63) Sauzade, M.; Pontnau, J.; Lesas, P.; Silhouette, D. *Phys. Lett.* **1966**, *19*, 617–618.
(64) Joyce, R. R.; Richards, P. L. *Phys. Rev.* **1969**, *179*, 375–380.